NASA Technical Paper 2878

1989

Benchmark Solutions for the Galactic Ion Transport Equations: Energy and Spatially Dependent Problems

Barry D. Ganapol
University of Arizona
Tucson, Arizona

Lawrence W. Townsend
and John W. Wilson
Langley Research Center
Hampton, Virginia

National Aeronautics and Space Administration
Office of Management
Scientific and Technical Information Division

Abstract

Nontrivial benchmark solutions are developed for the galactic ion transport (GIT) equations in the straight-ahead approximation. These equations are used to predict potential radiation hazards in the upper atmosphere and in space. Two levels of difficulty are considered: (1) energy independent and (2) spatially independent.

The analysis emphasizes analytical methods never before applied to the GIT equations. Most of the representations derived have been numerically implemented and compared with more approximate calculations. Accurate ion fluxes (to 3 to 5 digits) are obtained for nontrivial sources. For monoenergetic beams, both accurate doses and fluxes are found. The benchmarks presented herein are useful in assessing the accuracy of transport algorithms designed to accommodate more complex radiation protection problems. In addition, these solutions can provide fast and accurate assessments of relatively simple shield configurations.

1.0. Introduction

As mankind turns its attention toward establishing orbiting space stations to serve as bases for future space exploration, the protection of personnel against radiation has become a relevant issue. In the upper atmosphere and in space, high-energy heavy ions originating in deep space or in the Sun are a major source of penetrating particles. Not only is the unscattered contribution of concern, but also the secondary particles generated from direct nuclear or coulombic collisions can account for a significant fraction of the absorbed dose. To ensure proper shielding of space bases and interplanetary vehicles, predictive dose and flux computations must be developed. Monte Carlo methods that numerically simulate particle motion are important calculational tools; unfortunately, however, these methods require extensive computational resources for adequate accuracy and, therefore, cannot be routinely applied. With recent advances in numerical methods and computational strategies, deterministic methods characterized by the Boltzmann equation have become competitive to Monte Carlo simulations. For this reason, an effort has been initiated within NASA to develop reliable, multidimensional, deterministic methods for shield design.

One component of this effort has been directed toward the assessment of the accuracy of proposed deterministic algorithms. The "partial" verification of a given algorithm can be obtained by comparison with standard solutions of the governing equations. These solutions, referred to as *benchmarks,* are highly accurate numerical evaluations of simplified transport problems which, nevertheless, contain the physical features of the basic transport processes. The motivation behind such comparisons is that algorithms developed for realistic problems must also yield reliable results for these simple problems as well. Comparisons with benchmark solutions are just one component in the verification process. Others include particle conservation, following proper intuitive physical trends, and comparisons of results with those obtained from alternative algorithms designed for similar transport problems. Even with these additional components, only partial verification is achieved because each application is unique.

In this report, benchmarks for the straight-ahead Boltzmann equation describing ion transport in matter are developed. Particular emphasis is placed on the analytical techniques used to solve the coupled ordinary differential transport equations. The approach taken is to investigate simplified problems, eventually leading to consideration of the full set of galactic ion transport (GIT) equations. The current work is devoted to two problems, energy-independent and spatially independent problems. A full analysis is performed for each problem, with results for physically interesting cases included. In this way, the knowledge gained at each stage of the investigation can be employed in the next. Although the major emphasis herein is on the development of accurate numerical evaluations, the solutions obtained can also be used to provide an approximate characterization for realistic transport situations.

2.0. Galactic Ion Transport (GIT) Equations

Because of the high energy of the galactic ions (10 to 10^7 MeV), the straight-ahead approximation can be introduced into the Boltzmann equation with a high degree of confidence. In this approximation, ions are not angularly deflected; and, as the colliding ions break up in nuclear fragmentation, the fragments continue in the incident ion direction. Thus, for ions of charge number j, the appropriate transport equation is (ref. 1)

$$\left[\frac{\partial}{\partial x} - \frac{\partial}{\partial E}S_j(E) + \sigma_j(E)\right]\phi_j(x,E) = \sum_{k=j+1}^{J} m_{jk}(E)\sigma_k(E)\phi_k(x,E) \qquad (1a)$$

where ϕ_j is the flux of the jth ion at position x with energy per nucleon of E. (A list of symbols appears after the references.) The *macroscopic* absorption cross section is σ_j, m_{jk} is the multiplicity of ion

j produced in collision with ion k, and S_j is the absolute value of the change in energy E per unit distance traveled (i.e., the stopping power). The added assumption that target ion fragmentation can be neglected (ref. 1) is made in equation (1a). For most (but not all) cases studied, a homogeneous semiinfinite medium with a source at the free surface,

$$\phi_j(0, E) = f_j(E) \tag{1b}$$

is assumed.

As each benchmark is developed, additional assumptions appropriate to that benchmark are made. Also, in certain instances the restriction to a homogeneous shield is relaxed.

3.0. Energy-Independent Benchmark

3.1. Theory

We may obtain the energy-independent benchmark from the Boltzmann equations (1a) and (1b) by first assuming that the cross sections and fragmentation multiplicities are constants (independent of E). Equations (1) are then integrated over all energies to yield

$$\left(\frac{\partial}{\partial x} + \sigma_j\right)\phi_j(x) = \sum_{k=j+1}^{J} \beta_{jk}\phi_k(x) \tag{2}$$

and

$$\phi_j(0) = \delta_{jJ} \tag{3}$$

where the energy-independent flux is given by

$$\phi(x) = \int_0^\infty \phi_j(x, E)\, dE \tag{4}$$

and

$$\beta_{jk} = m_{jk}\sigma_k \tag{5}$$

A source of only J ions on the free surface has been specified. Equations (2) and (3) are solved with three different methods: (1) direct analytical solution, (2) Laplace transformation, and (3) power series expansion. Equation (2) is also applicable to a heterogeneous medium with spatially varying cross sections. This is accomplished by interpreting x as an optical thickness rather than as a linear thickness.

3.1.1. Direct analytical solution

Since equation (2) is nothing more than a set of coupled, ordinary differential equations, the general solution is a linear combination of exponentials. For example, for $j = J$ we have equations (2) and (3) reducing to

$$\left(\frac{\partial}{\partial x} + \sigma_J\right)\phi_J(x) = 0 \tag{6}$$

and

$$\phi_J(0) = 1 \tag{7}$$

The appropriate solution to equations (6) and (7) is therefore

$$\phi_J(x) = \exp(-\sigma_J x) \tag{8}$$

For $j = J - 1$ we have

$$\left(\frac{\partial}{\partial x} + \sigma_{J-1}\right)\phi_{J-1}(x) = \beta_{J-1,J}\phi_J(x) \tag{9}$$

with

$$\phi_{J-1}(0) = \delta_{J-1,J} = 0 \tag{10}$$

Now equation (9) is of the general form

$$\frac{dy}{dx} + P(x)y = Q(x) \tag{11}$$

which can be solved using an integrating factor as

$$y = \exp\left[-\int P(x)\, dx\right]\left\{\int Q(x)\exp\left[\int P(x)\, dx\right]dx\right\} + C\exp\left[-\int P(x)\, dx\right] \tag{12}$$

Because

$$y = \phi_{J-1}(x)$$
$$P(x) = \sigma_{J-1}$$

and

$$Q(x) = \beta_{J-1,J}\phi_J(x) = \beta_{J-1,J}\exp(-\sigma_J x)$$

the solution of equation (9) is

$$\begin{aligned}
&\phi_{J-1}(x) \\
&= \exp(-\sigma_{J-1}x)\left[\int \beta_{J-1,J}\phi_J(x)\exp(\sigma_{J-1}x)\, dx\right] \\
&\quad + C\exp(-\sigma_{J-1}x) \\
&= \exp(-\sigma_{J-1}x)\beta_{J-1,J}\int \\
&\quad \times \exp(-\sigma_J x)\exp(\sigma_{J-1}x)\, dx \\
&\quad + C\exp(-\sigma_{J-1}x) \\
&= \exp(-\sigma_{J-1}x)\beta_{J-1,J}\int \exp(\sigma_{J-1} - \sigma_J)x\, dx \\
&\quad + C\exp(-\sigma_{J-1}x) \\
&= \frac{\beta_{J-1,J}}{\sigma_{J-1} - \sigma_J}\exp(-\sigma_{J-1}x)\exp[(\sigma_{J-1} - \sigma_J)x] \\
&\quad + C\exp(-\sigma_{J-1}x) \\
&= \frac{\beta_{J-1,J}}{\sigma_{J-1} - \sigma_J}\exp(-\sigma_J x) + C\exp(-\sigma_{J-1}x)
\end{aligned} \tag{13}$$

Now, applying equation (10) to (13) yields

$$\phi_{J-1}(0) = 0 = \frac{\beta_{J-1,J}}{\sigma_{J-1} - \sigma_J} + C$$

which implies that

$$C = -\frac{\beta_{J-1,J}}{\sigma_{J-1} - \sigma_J}$$

Equation (13) thus becomes simply

$$\phi_{J-1}(x) = \frac{\beta_{J-1,J}}{\sigma_{J-1} - \sigma_J}[\exp(-\sigma_j x) - \exp(-\sigma_{J-1}x)] \tag{14}$$

From a constructive inductive proof, the general solution to equation (2) is

$$\phi_{J-l}(x) = \sum_{i=0}^{l} \alpha_{i,J-l} \exp(-\sigma_{J-i}x) \qquad (0 \le l \le J-1) \tag{15}$$

where the coefficients are given recursively by

$$\alpha_{0,J} = 1 \tag{16a}$$

$$\alpha_{i,J-l} = \sum_{k'=i}^{l-1} \frac{\beta_{J-l,J-k'}}{\sigma_{J-l} - \sigma_{J-i}} \alpha_{i,J-k'} \qquad (0 \le i \le l-1) \tag{16b}$$

$$\alpha_{l,J-l} = -\sum_{i=0}^{l-1} \alpha_{i,J-l} \tag{16c}$$

The last expression for $\alpha_{l,J=l}$ is required to satisfy the boundary condition (eq. (3))

$$\phi_j(0) = 0 \qquad (1 \le j \le J-1) \tag{17}$$

Because of the recurrence relation given by equations (16), the expression for $\phi_{J-l}(x)$ in equation (15) is susceptible to round-off error when J is large, and this error could be a significant numerical limitation. This direct analytical method is also applied to the energy-dependent benchmark.

3.1.2. Numerical Laplace transform inversion

Applying the Laplace transform

$$\tilde{\phi}_j(p) = \int_0^\infty dx \, \exp(-px)\phi_j(x) \tag{18}$$

to equations (2) and (3) yields

$$\tilde{\phi}_j(p) = \frac{1}{p + \sigma_j}\left[\delta_{jJ} + \sum_{k=j+1}^{J} \beta_{jk}\tilde{\phi}_k(p)\right] \tag{19}$$

Thus, an algebraic recurrence relation for the transformed flux has been established. This recurrence relation is most conveniently used in a numerical inversion procedure based on a decomposition of the Bromwich inversion integral into an infinite series, with application of the Euler-Knapp transformation to accelerate its convergence. When J is large, however, this procedure is expected to require excessive computational time as a result of the large number of transformed function evaluations ($\tilde{\phi}_j(p)$) required for the numerical integration.

3.1.3. Power series expansion

The least complicated solution method is based on a simple power (Taylor) series expansion of the form

$$\phi_j(x) = \exp(-\Gamma x) \sum_{n=0}^{\infty} \frac{x^n}{n!} h_{n,j} \tag{20}$$

Introducing this representation into equation (2) yields

$$\frac{\partial \phi_j}{\partial x} = -\Gamma \exp(-\Gamma x) \sum_{n=0}^{\infty} \frac{x^n}{n!} h_{n,j} + \exp(-\Gamma x) \sum_{n=0}^{\infty} \frac{x^{n-1}}{(n-1)!} h_{n,j}$$

so that

$$\sum_{n=0}^{\infty} \frac{x^{n-1}}{(n-1)!} h_{n,j} = \sum_{n=0}^{\infty} \frac{x^n}{n!}\left[-(\sigma_j - \Gamma)h_{n,j} + \sum_{k=j+1}^{J} \beta_{jk} h_{n,k}\right]$$

Equating coefficients of like powers of x yields the recurrence relation

$$h_{n+1,j} = -(\sigma_j - \Gamma)h_{n,j} + \sum_{k=j+1}^{J} \beta_{jk} h_{n,k} \tag{21}$$

From equation (20) we note that

$$\phi_j(0) = \delta_{jJ} = h_{0,j} \tag{22}$$

The introduction of the multiplicative exponential factor $\exp(-\Gamma x)$ in equation (20) is used to speed up

convergence of the power series in neutron transport calculations, but is not required here ($\Gamma = 0$).

A variant of the above expansion which can be used to further speed up convergence for large x is obtained by partitioning the slab into intervals. These intervals may be chosen to correspond to different shield materials or chosen for computational convenience. For the ith interval, defined as $a_{i-1} \leq x \leq a_i$, the following expansion is made:

$$\phi_j^i(x) = \sum_{n=0}^{\infty} \frac{(x - a_{i-1})^n}{n!} h_{n,j}^i \tag{23}$$

The recurrence relations for $h_{n,j}^i$, found in an analogous manner to those obtained in equations (21) and (22), are

$$h_{0,j}^i = \phi_j^{i-1}(a_{i-1}) \tag{24}$$

and

$$h_{n+1,j}^i = -\sigma_j^i h_{n,j}^i + \sum_{k=j+1}^{J} \beta_{jk} h_{n,k}^i \tag{25}$$

Equation (24) merely asserts that the flux incident on the ith slab is that which exits the $i - 1$ slab. Again, one must be alert to potential round-off error when using equations (20) to (25).

3.2. Numerical Implementation

In order to numerically compare the above solution methods, the following simplified nuclear model is assumed:

$$\sigma_j \equiv \sigma_o j^{2/3} \tag{26}$$

$$\left.\begin{aligned} m_{jk} &= \frac{2}{k-1} && (k \geq j) \\ &= 0 && (k < j) \end{aligned}\right\} \tag{27}$$

The choice of σ_j is based on the liquid drop model of nuclear physics. The multiplicities are chosen so as to conserve charge in each interaction.

3.2.1. Solution comparisons

Table I displays a comparison of the total flux

$$\phi_T(x) \equiv \sum_{j=1}^{J} \phi_j(x) \tag{28}$$

calculated using analytical and power series expansion methods for incident manganese ions ($J = 25$) colliding with an air shield ($\sigma_o = 0.01247$ cm^2/g) 100 g/cm^2 thick.

In the power series method, adequate convergence is obtained when the sum of three individual terms yields a relative error less than some desired amount ε_T. In the table, the total fluxes for four relative errors are shown compared with the fluxes for the analytical solution. The underlined digits are those in disagreement with the analytical solution. *All* power series calculations are within the specified relative errors. The power series method, however, takes approximately twice the computational time of the analytical method. In most respects the two methods are the same, except that the power series is more easily applied to heterogeneous shields. Also, and possibly more importantly, if round-off error becomes a problem, there is a readily available remedy for the power series expansion (multilayer treatment) but not for the analytical solution method.

A comparison of the analytical solution with the numerical Laplace transform inversion (at $x = 100$ g/cm^2) for different relative errors ε_L is displayed in table II. For 5-digit accuracy, the numerical inversion approach is inferior to the analytical or power series solution methods as it requires about 800 times the computational effort. Because of this computational inefficiency, the numerical inversion is not considered further for this benchmark.

Several physical trends are displayed in figures 1(a) and 1(b). Figure 1(a) shows the variation with x of the 25 species. As anticipated, the flux increases with decreasing j. This, of course, is a result of the increased fragmentation with increasing depth x as the ions penetrate farther and undergo more collisions. In figure 1(b), the variation of $\phi_T(x)$ with x is shown. Beyond $x = 100$ g/cm^2, ϕ_T begins to decrease and eventually becomes zero at infinity (large x). This is a physical requirement since all species have nonzero absorption cross sections, a fact which implies that each species must eventually disappear.

3.2.2. Multilayer formulation

The flux at 50 locations within a 100 g/cm^2 atmospheric shield was determined for both a single layer and for 5 layers each with 10 locations. The computational time for the five-layer calculation was about three-tenths of the time for the single layer, which indicates a clear advantage to using the multilayer formulation. As displayed in figures 2(a) and 2(b), the major advantage of the multilayer formulation is the more rapid convergence in each new layer. In these figures, the number of terms required for convergence N_{conv} (for $\varepsilon_T = 10^{-4}$) for the flux of the last-generated ion $\phi_1(x)$ is shown for both single-layer and five-layer configurations. A maximum of 10 terms are

required for the 5-layer calculation, whereas 23 terms are required for the single-layer calculation. This accounts for the previously mentioned reduction in computational time. This time advantage will, however, become a time disadvantage as the number of layers increases because of the associated increase in overhead. Another, more subtle, advantage of the multilayered formulation is the mitigation of round-off error by the accelerated convergence. If round-off error is suspected, or if the series does not converge within a specified number of terms, then more layers can be introduced to reduce the number of terms per layer required for convergence. Thus, fewer iterations of the recurrence relations are needed to provide more accurate values of $h_{n,j}$ to be used in the summation.

3.2.3. Comparison with other methods

A natural numerical approach to solution of equations (2) and (3) is the standard implicit numerical finite-difference scheme. If the shield is partitioned into N uniform intervals of width Δx and the derivative in equation (2) is approximated at the nth interval boundary by

$$\frac{d\phi_j(x)}{dx} \approx \frac{\phi_j^n - \phi_j^{n-1}}{\Delta x} \tag{29}$$

then the following recurrence relation ensues:

$$\phi_j^0 = \delta_{jJ} \tag{30}$$

$$\phi_j^{n+1} = \frac{1}{1+\Delta x\,\sigma_j}\left(\phi_j^n + \Delta x \sum_{k=j+1}^{J} \beta_{jk}\phi_k^{n+1}\right) \tag{31}$$

In table III, the total flux (eq. (28)) obtained from this implicit discretized formulation is compared to the analytical result for decreasing Δx (increasing N). Surprisingly, better than 5-percent accuracy is obtained for 20 intervals and 0.1-percent accuracy for 160 intervals. In addition, the correct result is approached as Δx decreases. Thus, a finite-difference formulation can provide an acceptable numerical solution to the energy-independent GIT equations.

A second comparison is now made with a multiple collision (or perturbation) formulation developed in reference 1. The estimated percent differences between the multiple collision and analytical solutions are listed in table IV. Based upon the last neglected term, it is estimated that the multiple collision formulation is accurate to within 10 percent. This is clearly verified by the analytical benchmark comparison.

3.2.4. Selected case studies

3.2.4.1. Generation of ion $J+1$. Because of proton capture reactions, there is a finite probability that ion $J+1$ can be formed from ion J. To account for this, an equation for ion $J+1$ must be considered. Therefore, equation (2) becomes

$$\left(\frac{\partial}{\partial x} + \sigma_{J+1}\right)\phi_{J+1}(x) = C_+\phi_J(x) \tag{32}$$

and

$$\left(\frac{\partial}{\partial x} + \sigma_j\right)\phi_j(x) = \sum_{k=j+1}^{J+1} \beta_{jk}\phi_k(x) \tag{33}$$

where the sum in equation (33) now includes $J+1$, since it can fragment into lighter ions ($1 \le j \le J$) after it is formed. Equations (32) and (33) are most easily solved with the power series expansion to give

$$h_{0,j}^i = \phi_j^{i-1}(a_{i-1}) \tag{34a}$$

$$h_{n,J+1}^i = -\sigma_{J+1}h_{n-1,J+1}^i + C_+h_{n-1,J}^i \tag{34b}$$

$$h_{n,j}^i = -\sigma_J h_{n-1,J}^i + \beta_{J,J+1}h_{n-1,J+1}^i \tag{34c}$$

and

$$h_{n,j}^i = -\sigma_j h_{n-1,J}^i + \sum_{k=j+1}^{J+1} \beta_{jk}h_{n-1,k}^i \tag{34d}$$

Figures 3 and 4 show the influence of C_+ on the total flux equation (28) with J replaced by $J+1$ and on $\phi_{J+1}(x)$. The most probable value for C_+ is about 0.01 so that the generation of ion $J+1$ does not have a significant impact on ϕ_T. If C_+ increases to about 0.1, however, then the production of ion $J+1$ can become important. Figure 4 shows the expected reduction in ϕ_{J+1} profile with decreasing C_+.

3.2.4.2. Multiple shields. The total flux for a composite shield of 10 layers with differing density factors relative to air are displayed in figure 5. As is apparent in the low-density shields (5, 7, and 10), the total flux remains nearly constant because of the reduced collision probability. For the high-density shields (4, 6, and 8), the flux changes rapidly because of the increased fragmentation probability. In shield 4, the flux initially increases (because of fragmentation) but then decreases because of the predominance of absorption.

4.0. Spatially Independent Benchmark

4.1. Theory

A spatially independent benchmark is easily derived by considering cross sections and multiplicities

as spatially constant and treating the boundary condition as a volume source. For a monoenergetic source of ions J, equations (1a) and (1b) become

$$\left[\frac{\partial}{\partial x} - \frac{\partial}{\partial E}S_j(E) + \sigma_j(E)\right]\phi_j(x,E) = \sum_{k=j+1}^{J}\beta_{jk}(E)\phi_k(x,E) + \delta(x)\delta(E)\delta_{jJ} \tag{35a}$$

and

$$\phi_j(0,E) = 0 \tag{35b}$$

Integrating over the half-space $(0 \rightarrow \infty)$ and defining

$$\phi_j(E) = \int_0^\infty \phi_j(x,E)\,dx \tag{36}$$

yields the desired spatially independent ion transport equations

$$\left[-\frac{\partial}{\partial E}S_j(E) + \sigma_j(E)\right]\phi_j(E) = \sum_{k=j+1}^{J}\beta_{jk}(E)\phi_k(E) \tag{37a}$$

and

$$\phi(E_o) = \frac{\delta_{jJ}}{S_J(E_o)} \tag{37b}$$

The volume source has been transformed into an initial condition in energy by our integrating over an infinitesimal interval about E_o and noting that $\phi(E)$ at the upper bound is zero since upscattering is not allowed.

At this point, it becomes convenient to introduce a well-known scaling law between stopping powers at high energies:

$$S_j(E) = \nu_j S_p(E) \tag{38}$$

where

$$\nu_j \equiv \frac{Z_j^2}{A_j} \tag{39}$$

and S_p is the proton stopping power, S_j is the stopping power of the jth ion, Z_j is the charge number of the jth ion, and A_j is the atomic mass of the jth ion. With this substitution and variables changed from energy to proton path length traveled at a given energy ($s(E,E_o)$), equations (37a) and (37b) become

$$\left[\nu_j\frac{\partial}{\partial s} + \sigma_j(s)\right]\phi_j(s) = \sum_{k=j+1}^{J}\beta_{jk}(s)\phi_k(s) \tag{40a}$$

and

$$\phi_j(0) = \frac{\delta_{jJ}}{\nu_J} \tag{40b}$$

where the path length is given by

$$s(E,E_o) = \int_E^{E_o}\frac{dE'}{S_p(E')} \tag{41}$$

which, from the definition of the flux distribution, implies

$$\phi_j(x,s) \equiv S_p(E)\phi_j(x,E) \tag{42}$$

The major difficulty in applying the above transformations is the use of equation (41) to determine the path length s from the energy E since an integral must be inverted to return to the energy-dependent flux of equation (42). This added inconvenience, however, is readily acceptable because of the enormous simplification offered by the energy and path length transformation. Indeed, equation (40) now closely resembles the energy-independent case, and similar solution methods can therefore be adopted.

4.1.1. Analytical flux solution and dose

As before, an analytical solution can be found for constant multiplicities and cross sections. By casting equations (40a) and (40b) in the form of equations (2) and (3), the solution becomes (from section 3.1.1)

$$\phi_{J-l}(s) = \sum_{i=0}^{l}\alpha_{i,J-l}\exp(-\sigma_{J-i}s/\nu_{J-i}) \qquad (l = 0,\ 1,\ \ldots,\ J-1) \tag{43}$$

where

$$\alpha_{0,J} = \frac{1}{\nu_J} \tag{44a}$$

$$\alpha_{i,J-l} \equiv \left[\frac{1}{(\sigma_{J-l}/\nu_{J-l}) - (\sigma_{J-i}/\nu_{J-i})}\right] \times \frac{1}{\nu_{J-l}}\sum_{k=J-i}^{J-l+1}\beta_{J-l,k}\alpha_{i,k} \qquad (0 \le i \le l-1) \tag{44b}$$

$$\alpha_{l,J-l} = -\sum_{i=0}^{l-1}\alpha_{i,J-l} \tag{44c}$$

To treat explicit energy dependence of σ_j and m_{jk}, a piecewise constant assumption, or interval formulation, similar to the multigroup approximation of neutron transport theory is made. The path length (or energy) variable is partitioned, with constant transport properties assumed within each interval

(or group). Equations (40a) and (40b) can then be written in each interval as

$$\left(\nu_j \frac{\partial}{\partial s} + \sigma_j^r\right) + \phi_j^r(s) = \sum_{k=j+1}^{J} \beta_{jk} \phi_k^r(s) \qquad (45a)$$

and

$$\phi_j^r(a_{r-1}) = \phi_j^{r-1}(a_{r-1}) \quad (a_{r-1} \le s \le a_r) \qquad (45b)$$

where continuity of the flux is maintained across each interval interface. The quantities σ_j^r and β_{jk}^r are the appropriate transport coefficients averaged over the rth interval. Again, the solution is of the form given in equation (43) as (for the rth interval)

$$\phi_{J-l}^r(s) = \sum_{i=0}^{l} \alpha_{i,J-l}^r \exp(-\sigma_{J-i}^r s/\nu_{J-i}) \qquad (l = 0,\ 1,\ \ldots,\ J-1) \qquad (46)$$

with

$$\alpha_{i,J-l}^r = \left[\frac{1}{(\sigma_{J-l}^r/\nu_{J-l}^r) - (\sigma_{J-i}^r/\nu_{J-i}^r)}\right]\left(\frac{1}{\nu_{J-l}^r}\right) \times \sum_{k=J-i}^{J-l+1} \beta_{J-l,k}^r \alpha_{i,k}^r \qquad (0 \le i \le l-1) \qquad (47)$$

for each interval r. For $i = l$, we have

$$\alpha_{l,J-l}^r = \phi_{J-l}^{r-1}(a_{r-1}) - \sum_{i=0}^{l-1} \alpha_{i,J-l}^r \qquad (48)$$

This formulation is completely analogous to the spatial multilayer formulation discussed in section 3.1.3.

With this particular form of the analytical solution, the evaluation of dose becomes relatively simple. The usual expression for the energy deposited by ion j is

$$D_j(E) = A_j \int_0^{E_o} dE\, S_j(E) \phi_j(E) \qquad (49)$$

which can also be written as

$$D_j(E) = \nu_j A_j \int_0^{E_o} dE\, \phi_j[s(E, E_o)] \qquad (50)$$

From the partitioned nature of s, and therefore E, we have

$$D_j = \nu_j \sum_{r=1}^{N_r} \int_{E_r}^{E_{r-1}} dE\, \phi_j^r[s(E, E_o)] \qquad (51)$$

Substituting equation (46) for each interval gives

$$D_j = \nu_j A_j \sum_{r=1}^{N_r} \sum_{i=0}^{J-j} \alpha_{ij}^r \int_{E_r}^{E_{r-1}} dE \times \exp\left[-\sigma_{j-i}(s - a_{r-1})/\nu_{J-i}\right] \qquad (52)$$

To perform the indicated integrations, an explicit relation between s and E (eq. (41)) must be specified. The analysis is somewhat simplified, however, if the following analytical range-energy relations (ref. 2) are used:

$$s(E_o, E) = R(E_o) - R(E) \qquad (53)$$

where

$$R(E) \equiv \alpha_o \ln(1 + \alpha_1 E^{n_o}) \qquad (54)$$

The term $R(E_o)$ is actually the maximum proton range. Inverting equation (53) for E gives

$$E = \left[\left(\exp\left\{\left[R(E_o) - s\right]/\alpha_o\right\} - 1\right)/\alpha_1\right]^{1/n_o} \qquad (55)$$

The expression for D_j given by equation (52) can therefore be simplified to

$$D_j = \nu_j A_j \sum_{r=1}^{N_r} \sum_{i=0}^{J-j} \alpha_{ij}^r \int_{E_r}^{E_{r-1}} dE \times \left(\frac{1 + \alpha_1 E^{n_o}}{1 + \alpha_1 E_{r-1}^{n_o}}\right)^{\alpha_o \sigma_{j-i}/\nu_{J-i}} \qquad (56)$$

4.1.2. Power series expansion

If piecewise constant transport properties are assumed, a formulation identical to the multilayer solution developed in section 3.1.3 can be employed. Following that same solution procedure, we assume the expansion

$$\phi_j^r(x) = \sum_{n=0}^{\infty} \frac{(s - s_{r-1})^n}{n!} h_{n,j}^r \qquad (57)$$

which, when substituted into equations (45), yields

$$h_{0,j}^r = \phi_j^{r-1}(s_{r-1}) \qquad (58)$$

and

$$h_{n+1}^r = \frac{1}{\nu_j}\left(-\sigma_j^r h_{n,j}^r + \sum_{k=j+1}^{J} \beta_{jk} h_{n,k}^r\right) \qquad (59)$$

The dose can be determined from equation (51) as

$$D_j = \nu_j A_j \sum_{n=0}^{\infty} \sum_{r=1}^{N_r} \frac{h_{n,j}^r}{n!} \int_{E_r}^{E_{r-1}} dE\,(s - a_{r-1})^n \quad (60)$$

which, upon insertion of the range-energy relations (eqs. (53) and (54)) becomes

$$D_j = \nu_j A_j \sum_{n=0}^{\infty} \sum_{r=1}^{N_r} \frac{h_{n,j}^r}{n!} \times \alpha_o^n \int_{E_r}^{E_{r-1}} dE \ln \left(\frac{1 + \alpha_1 E_{r-1}^{n_o}}{1 + \alpha_1 E^{n_o}} \right)^n \quad (61)$$

Not only are these integrals more complicated than those for the analytical result (eq. (56)), but also there are typically more of them to evaluate, making the power series expansion method less attractive for calculating doses.

4.2. Distributed Sources

For a single ion source of type J at the boundary,

$$\tilde{\phi}_j(0, E) = \delta_{jJ} \tilde{f}(E) \quad (62)$$

The spatially independent benchmark is again obtained by integrating equation (35a) over x to yield

$$\left[-\frac{\partial}{\partial E} S_j(E) + \sigma_j \right] \tilde{\phi}_j(E) = \sum_{k=j+1}^{J} \beta_{jk} \tilde{\phi}_k(E) + \delta_{jJ} \tilde{f}(E) \quad (63)$$

Changing to the path length variable and using equations (38) and (39) we find

$$\left[\nu_j \frac{\partial}{\partial s} + \sigma_j(s) \right] \tilde{\phi}_j(s) = \sum_{k=j+1}^{J} \beta_{jk} \tilde{\phi}_k(s) + \delta_{jJ} f(s) \quad (64)$$

where

$$f(s) = S_p(E) \tilde{f}(E) \quad (65)$$

With the Green's function found in the preceding two sections, the solution is obtained as the following convolution integral:

$$\tilde{\phi}_j(s) = \int_0^s du\, f(s - u) \phi_j(u) \quad (66)$$

and from the analytical and power series solutions, one can therefore write the following equations for a single region:

$$\tilde{\phi}_j(s) = \sum_{i=0}^{J-j} \alpha_{ij} \int_0^s du\, f(s - u) \times \exp(-\sigma_{J-i} u / \nu_{J-i}) \quad (67)$$

and

$$\tilde{\phi}_j(s) = \sum_{n=0}^{\infty} \frac{h_{n,j}^r}{n!} \int_0^s du\, f(s - u) u^n \quad (68)$$

The integrals in equations (67) and (68) can be costly to evaluate numerically; therefore, the method with the fewest number of integrals is preferable. In most instances, the analytical formulation requires the least computational effort.

Another very effective approximate solution, for general distributed sources, can be obtained with the multigroup or interval formulation technique. (See section 4.1.1.) If the source is averaged over the path length interval $r(f_j^r)$, an analytical solution can again be found in the form

$$\tilde{\phi}_{J-l}^r(s) = \Lambda_{J-l}^r + \sum_{i=0}^{l} \tilde{\alpha}_{i,J-l}^r \times \exp\left[-\beta_{J-i}(s - a_{r-1}) \right] \quad (69)$$

where

$$\beta_{J-i} \equiv \frac{\sigma_{j-i}}{J_{j-i}}$$

This solution is established by finding the particular solution for a constant source and adding it to the homogeneous solution. The coefficients $\tilde{\alpha}_{i,j-l}^r$ and the additive term Λ_{j-l}^r are now more complicated, but they can still be found recursively as follows:

$$\tilde{\alpha}_{0,J}^r = f_J^r - \frac{f_J^r}{\nu_J \beta_J^r} \quad (70a)$$

$$\Lambda_J^r = \frac{f_J^r}{\beta_J^r \nu_J} \quad (70b)$$

$$\tilde{\alpha}_{l,J-l}^r = f_{J-l}^r - \Lambda_{J-l}^r - \sum_{i=0}^{l-1} \tilde{\alpha}_{i,J-l}^r \quad (70c)$$

$$\Lambda_{J-l}^r = \frac{1}{\beta_{J-l}^r \nu_{J-l}} \times \left(f_{J-l}^r + \sum_{i=0}^{l-1} \beta_{J-l,J-i}^r \Lambda_{J-i}^r \right) \quad (70d)$$

with $\tilde{\alpha}_{i,J-l}^r$ given by equation (44a) for $0 \le i \le l - 1$ within each interval r. This procedure can be continued for any polynomial variation of the

source, although the algebra becomes increasingly more difficult and cumbersome: Because of this algebraic complexity, only analytical solutions for constant sources are considered.

The power series expansion, however, is more easily extended to other polynomial sources. For example, for a quadratic source distribution,

$$f_J^r(s) = Q_0^r + Q_1^r(s - a_{r-1}) + Q_2^r(s - a_{r-1})^2 \quad (71)$$

only the term

$$\frac{\delta_{iJ}}{\nu_J}\left(Q_0^r\delta_{n,1} + Q_1^r\delta_{n,2} + Q_2^r\delta_{n,3}\right)$$

need be added to the right-hand side of equation (59) to give the appropriate $\tilde{h}_{n,j}^r$.

4.3. Numerical Implementation

4.3.1. Flux solution comparisons

Table V provides a comparison of $\phi_1(E)$ as given by the analytical and power series expansion solutions with $J = 25$ and $E_o = 5$ GeV. For the remainder of this work, the nuclear properties given by equations (26) and (27) are utilized unless otherwise stated. As shown in the table, the power series solution does not uniformly approach the analytical solution as the truncation error is decreased from 0.01 to 0.0001. This failure is apparently a result of round-off error, as implied by the evaluation of $h_{n,j}^r$ in double precision, for which most of the ϕ_1 values compare better with the analytical ones. This error is eliminated when the same energy region is partitioned into 4 intervals with 10 points per interval. As shown in the table, the four-interval double-precision and analytical results are identical. The reason for this is clearly that fewer terms are required for convergence, thereby reducing the inaccuracies introduced into the calculated coefficients $h_{n,j}^r$ (section 3.2.2). To reduce the prospect of round-off error being a problem in determining α_{ij} and $h_{n,j}^r$, these coefficients are calculated with double-precision arithmetic.

Figure 6 displays the ion flux variations with energy. The flux typically increases with decreasing j (for a given energy), as the number of fragmentation interactions increases the secondary particle production.

4.3.2. Dose calculations

The dose calculations appear to be less accurate and reliable than the flux calculations. In table VI, the ion dose factors computed with the analytical solution (eq. (56)) are displayed for decreasing relative error of the numerical Romberg integration scheme (ref. 3). Convergence to only two significant figures is achieved. This lack of accuracy, resulting from accumulated round-off error of equation (56), occurs because subtraction of large numbers eventually yields relatively small numerical values. Any variation in these large numbers resulting from reductions in the integration error produces differing results. For $J = 10$, however, table VII shows that the calculated doses do converge. Therefore, we conclude that the dose calculation is useful as a tabulated benchmark only if few ions are involved (less than 10); otherwise, only graphical comparisons should be made. Figure 7 displays such a comparison for various initial energies E_o. As E_o increases, the lighter ions begin to contribute significantly to the total dose

$$D_T = \sum_{j=1}^{J} D_j \quad (72)$$

since higher E_o implies that more fragmentations occur.

4.3.3. Distributed sources

4.3.3.1. Benchmark source. To illustrate the application of the convolution integral (eq. (66)) to generating benchmark data, a simple exponential source of the form

$$f(s) = \exp(-a_o s) \quad (73)$$

is considered. In the energy variable, this source corresponds to

$$f(E) = [S_p(E)]^{-1}\frac{1 + \alpha_1 E^{n_o}}{1 + \alpha_1 E_o^{n_o}} a_o\alpha_o \quad (74)$$

For this particular source, the integration in equation (67) can be analytically performed to yield

$$\tilde{Q}_j(s) = \sum_{i=0}^{J-j} \alpha_{ij}\left[\exp(-\beta_{J-i}s) - \exp(-a_o s)\right](\beta_{J-i} - a_o) \quad (75)$$

For an exponential source of manganese ions ($J = 25$) in air, the rapid variation of ϕ_1 with a_o is displayed in figure 8. As shown in figure 9, the energy variation of the flux for all species follows that of the source ions. Since all calculations involve well-known, online functions, no convergence problems are experienced for this source type. Therefore, the convolution integral appears to be an efficient way to generate reliable results for a class of sources for which the integral can be performed analytically.

4.3.3.2. Solar source. A significant source of heavy ions is the Sun. The approximate energy dependence is given by (ref. 4)

$$f(E) = \frac{b_o}{(b_1 + E)^n} \tag{76}$$

where b_o, b_1, and n are parameters. For both analytical and power series solution methods, interval options are used to evaluate the flux from this source. The analytical results for an assumed constant source of $J = 25$ ions within an interval are displayed in figures 10(a) and 10(b) for 15 and 40 intervals spanning the energy range of 10 to 10^4 MeV per nucleon. There are two points taken per interval. With only 15 intervals, oscillations in the ion fluxes are clearly noticeable. When the number of intervals is increased, however, the oscillations are reduced (see fig. 10(b)). Similar smoothing effects are obtained for the power series solutions displayed in figures 11(a) to 11(c). Note that the quadratic source representation used for figure 11(c) provides fluxes free of oscillations.

To verify that the interval calculations are indeed giving accurate fluxes, the solar source is replaced by the exponential source from equation (73). Comparisons between $\tilde{\phi}_1$ calculated with the analytical interval methods and those values obtained from the benchmark source with $a_o = 0$ and 10^{-3} are displayed in figures 12(a) and 12(b). As is clearly shown, the results for $\tilde{\phi}_1$ are virtually identical for the two solution methods, and this agreement indicates that the interval calculation is sufficiently accurate to use in estimating fluxes from distributed sources.

4.3.4. Comparison with a finite-difference solution

A finite-difference scheme similar to the one developed for the first benchmark can be constructed. This scheme takes the following form for a delta function source:

$$\phi_j^0 = 1/\nu_j \tag{77}$$

and

$$\phi_j^g = \frac{1}{\nu_j + \Delta s\, \sigma_j^g} \left[\nu_j \phi_j^{g-1} + \Delta s \sum_{k=j+1}^{J} \beta_{jk}^g \phi_k^g \right] \tag{78}$$

and Δs is determined by dividing the interval $[0, R(E_o)]$ equally:

$$\Delta s = \frac{R(E_o)}{N_p} \tag{79}$$

where N_p is the number of intervals. In figures 13(a) to 13(d), the interval and analytical fluxes for the $j = 1$ ion are compared for decreasing Δs (increasing N_p). As Δs decreases, the interval solution does indeed approach the analytical solution, with excellent agreement at high energies ($E > 1$ GeV/amu). For lower energies, the agreement is acceptable but not spectacular. Because the majority of the dose is contributed by the high-energy flux, the interval calculation appears to provide an adequate means for dose characterization.

In an attempt to improve on the agreement at relatively low energies, a hybrid scheme utilizing both the analytical and interval solution methods was developed. In this approach, the analytical solution is used to obtain the flux for $j \geq J_0$ and the interval solution is used for $1 \leq j \leq J_0 - 1$. The summation in the interval solution (eq. (78)) is split into two sums

$$\sum_{k=j+1}^{J_0-1} \beta_{jk}^g \phi_k^g + \sum_{k=J_0}^{J} \beta_{jk}^g \phi_k^g$$

where the right-hand summation is obtained from the analytical solution. In figure 14, ϕ_1 is plotted for several values of J_0 when $N_p = 10$. A significant improvement over the original interval solution ($J_0 = 25$) is observed for low energies, even when only one analytical flux is used (i.e., $J_0 = 24$). For this last case, however, the flux at high energies is less accurate than that obtained for the original solution ($J_0 = 25$). As J_0 approaches 1, the solution continually improves. The discrepancy between $J_0 = 2$ and $J_0 = 1$ is entirely due to the finite-difference approximation. Improvement of this can be obtained only by increasing N_p.

The complete spectra for all ions using both analytical and interval solutions ($N_p = 100$) are displayed in figure 15. These calculations are in very good agreement, considering that the finite-difference scheme is crude and J is relatively large.

4.3.5. Energy-dependent absorption cross section

To demonstrate the energy-dependent absorption cross-section option, a functional form, as displayed in figure 16, has been assumed. This is similar to the actual cross-section shape (ref. 5). All ion cross sections are assumed to scale according to

$$\sigma_j(E) = j^{2/3} f_c(E) \tag{80}$$

The fluxes for all ions for cross sections with and without the energy dependence are displayed in figures 17(a) and 17(b). In general, the high-energy portion of the flux (above 1 GeV) is relatively unaffected by the energy dependence since the cross

sections are essentially constant there. At lower energies the fluxes are slightly higher for the energy-dependent cross sections, since $\sigma_j(E)$ is larger than the corresponding energy-independent values and, thus, there is a greater probability of interaction.

5.0. Concluding Remarks

Energy-independent and spatially independent benchmark solutions to the galactic ion transport (GIT) equations have been developed, and accurate ion fluxes have been obtained for realistic source representations. Analytical, power series, and Laplace transform inversion solution methods were developed. The analytical methods are limited only by round-off errors. The power series methods are approximately half as fast, computationally, as the analytical methods, but are more easily altered to correct round-off errors. The Laplace transform inversion methods are the least useful because of the excessive computational times necessary for handling the large number of different ions in the galactic cosmic ray spectrum. For monoenergetic laboratory beams both accurate fluxes and doses were found. Examples of applications to relatively simple shield configurations were also presented. The coupled GIT equations are partial differential equations which are, by their nature, more difficult to solve; nevertheless, an analytical solution can be found.

NASA Langley Research Center
Hampton, VA 23665-5225
January 12, 1989

6.0. References

1. Wilson, John W.: *Analysis of the Theory of High-Energy Ion Transport.* NASA TN D-8381, 1977.
2. Wilson, John W.; and Badavi, F. F.: Methods of Galactic Heavy Ion Transport. *Radiat. Res.*, vol. 108, 1986, pp. 231–237.
3. Miller, Alan R.: *FORTRAN Programs for Scientists and Engineers, 1st ed.* SYBEX, Inc., 1982.
4. Haffner, James W.: *Radiation and Shielding in Space.* Academic Press, Inc., 1967.
5. Townsend, Lawrence W.; and Wilson, John W.: *Tables of Nuclear Cross Sections for Galactic Cosmic Rays—Absorption Cross Sections.* NASA RP-1134, 1985.

7.0. Symbols

A_j	mass number of jth ion
a_i	position of ith interval boundary, g/cm^2
b_o, b_1	parameters used in equation (76)
C	arbitrary integration constant
C_+	probability of forming ion $J+1$
D_j	dose due to jth ion, MeV/g
D_T	total dose, defined in equation (72)
E	energy per nucleon, MeV/nucleon or MeV/amu
$f_c(E)$	energy-dependent absorption cross section
f_j	monoenergetic beam source term
$h^r_{n,j}, h_{n,j}$	power series coefficients
J	charge number of incident ion
j	charge number of jth ion
m_{jk}	multiplicity of ion j produced by ion k
N	number of intervals
N_{conv}	number of terms for convergence
$P(x), Q(x)$	arbitrary polynomials
Q^r_i	rth interval polynomial source coefficient ($i = 0, 1, 2$)
R	range, g/cm^2
S_j	stopping power of jth ion, MeV-cm^2/g
S_p	proton stopping power, MeV-cm^2/g
$s(E, E_o)$	proton path length, g/cm^2
x	position, g/cm^2
y	arbitrary, dependent variable
α_{ij}	recursion coefficient
α_o, α_1, n_o	parameters used in equation (54)
β_{jk}	$= m_{jk}\sigma_k$ (eq. (5))
Γ	convergence factor in equation (20), cm^2/g
Δs	$= \frac{R(E_o)}{N_p}$ (eq. (79))
Δx	interval width, g/cm^2
δ_{jJ}	Kronecker delta
ν_j	$= \frac{Z_j^2}{A_j}$ (eq. (39))
σ_j	macroscopic absorption cross section for jth ion, cm^2/g
σ_o	cross-section parameter, cm^2/g
ϕ_j	flux of jth ion
$\tilde{\phi}_j$	Laplace transform of ϕ_j
ϕ_T	total flux (eq. (28))

Table I. Total Flux Computations as Function of Atmosphere Thickness

Thickness, g/cm^2	Total flux (relative to incident flux) calculated with—				
		Power series expansion for—			
	Analytical solution	$\varepsilon_T = 0.01$ (a)	$\varepsilon_T = 0.001$ (a)	$\varepsilon_T = 0.0001$ (a)	$\varepsilon_T = 0.00001$
0	1.0000	1.0000	1.0000	1.0000	1.0000
1	2.1594	2.1594	2.1594	2.1594	2.1594
2	3.4522	3.4523	3.4522	3.4522	3.4522
3	4.8015	4.8013	4.8014	4.8015	4.8015
4	6.1375	6.1372	6.1375	6.1375	6.1375
5	7.4016	7.0423	7.4017	7.4016	7.4016
6	8.5479	8.5481	8.5479	8.5479	8.5479
7	9.5434	9.5434	9.5435	9.5435	9.5434
8	10.368	10.367	10.368	10.368	10.368
9	11.011	11.008	11.009	11.011	11.011
10	11.473	11.483	11.473	11.473	11.473

[a]Underlined digits are in disagreement with analytical solutions.

Table II. Relative Total Flux and Computation Times for Analytical and Numerical Inversion Solution Methods

[$x = 100$ g/cm^2]

Method	Total flux (relative to incident flux)	Computation times, CPU sec/point
Analytical	11.473	0.05
Numerical inversion:		
$\varepsilon_L = 0.1$	11.500	19.7
$\varepsilon_L = 0.01$	11.480	26.9
$\varepsilon_L = 0.001$	11.474	33.4
$\varepsilon_L = 0.0001$	11.473	39.2

Table III. Total Flux Computations Obtained From Analytical and Discretized Solution Methods as Function of Atmosphere Thickness

Thickness, g/cm^2	Total flux (relative to incident flux) from—					
	Analytical solution	Discretized solution for number of intervals of—				
		10	20	40	80	160
20	3.4522	3.4688	3.4695	3.4634	3.4585	3.4556
40	6.1375	5.9588	6.0550	6.0983	6.1186	6.1282
60	8.5479	8.1020	8.3219	8.4344	8.4911	8.5195
80	10.368	9.6984	10.019	10.019	10.278	10.322
100	11.473	10.686	11.059	11.260	11.365	11.418

Table IV. Relative Flux Differences Between Analytical and Multiple Collision Solutions as Function of Target Thickness

Thickness, g/cm^2	Percent difference
10	4.5
20	3.0
30	2.0
40	5.5
50	5.7
60	8.8

Table V. Values of ϕ_1 Determined From Analytical and Polynomial Expansion Solutions

$[J = 25;\ E_0 = 5\ \text{GeV}]$

Energy, MeV/nucleon	ϕ_1 from analytical solution	ϕ_1 from polynomial expansion solution for—				
		One interval (single precision) with an allowed truncation error of—			One interval (double precision)	Four intervals (double precision)
		0.01	0.001	0.0001		
10.000	1.3560E-03	1.3529E-03	1.3527E-03	1.3527E-03	1.3548E-03	1.3560E-03
18.616	2.2176E-03	2.2140E-03	2.2137E-03	2.2137E-03	2.2176E-03	2.2176E-03
34.657	3.6333E-03	3.6252E-03	3.6248E-03	3.6247E-03	3.6302E-03	3.6333E-03
64.520	5.9866E-03	5.9852E-03	5.9846E-03	5.9845E-03	5.9906E-03	5.9866E-03
120.11	1.0032E-02	1.0032E-02	1.0033E-02	1.0033E-02	1.0029E-02	1.0032E-02
223.61	1.7661E-02	1.7662E-02	1.7659E-02	1.7659E-02	1.7656E-02	1.7661E-02
416.28	3.5476E-02	3.5471E-02	3.5476E-02	3.5477E-02	3.5474E-02	3.5476E-02
774.96	9.4341E-02	9.4327E-02	9.4339E-02	9.4340E-02	9.4341E-02	9.4341E-02
1442.7	3.4442E-01	3.4438E-01	3.4442E-01	3.4442E-01	3.4442E-01	3.4442E-01
2685.8	8.8492E-01	8.8478E-01	8.8491E-01	8.8492E-01	8.8492E-01	8.8492E-01

Table VI. Dose Fraction Versus Ion Charge Number and Relative Integration Error for Manganese Ions Incident Upon Atmosphere

[E_o = 1000 MeV/nucleon]

Ion charge number	Dose fraction for relative integration error of—					
	10^{-2}	10^{-4}	10^{-6}	10^{-8}	10^{-10}	10^{-12}
1	5.3599E-01	4.4442E-01	5.3621E-01	5.3645E-01	5.3619E-01	5.3452E-01
2	1.1879E-01	1.3416E-01	1.1875E-01	1.1881E-01	1.1876E-01	1.1906E-01
3	5.9635E-02	6.9760E-02	5.9609E-02	5.9608E-02	5.9611E-02	5.9802E-02
4	4.1417E-02	4.9225E-02	4.1398E-02	4.1387E-02	4.1400E-02	4.1545E-02
5	3.0832E-02	3.7123E-02	3.0816E-02	3.0801E-02	3.0818E-02	3.0933E-02
6	2.5981E-02	3.1531E-02	2.5967E-02	2.5950E-02	2.5968E-02	2.6069E-02
7	2.0793E-02	2.5501E-02	2.0782E-02	2.0764E-02	2.0783E-02	2.0868E-02
8	1.7125E-02	2.1157E-02	1.7115E-02	1.7098E-02	1.7116E-02	1.7188E-02
9	1.3704E-02	1.7033E-02	1.3696E-02	1.3680E-02	1.3697E-02	1.3756E-02
10	1.2350E-02	1.5383E-02	1.2343E-02	1.2327E-02	1.2343E-02	1.2397E-02
11	1.0301E-02	1.2872E-02	1.0295E-02	1.0281E-02	1.0296E-02	1.0341E-02
12	9.4449E-03	1.1814E-02	9.4393E-03	9.4260E-03	9.4397E-03	9.4815E-03
13	8.1070E-03	1.0156E-02	8.1023E-03	8.0903E-03	8.1026E-03	8.1386E-03
14	7.5260E-03	9.4332E-03	7.5215E-03	7.5102E-03	7.5218E-03	7.5553E-03
15	6.5966E-03	8.2738E-03	6.5927E-03	6.5826E-03	6.5930E-03	6.6224E-03
16	6.1814E-03	7.7547E-03	6.1778E-03	6.1682E-03	6.1781E-03	6.2056E-03
17	5.5054E-03	6.9083E-03	5.5021E-03	5.4935E-03	5.5024E-03	5.5269E-03
18	4.7170E-03	5.9196E-03	4.7142E-03	4.7068E-03	4.7144E-03	4.7355E-03
19	4.6828E-03	5.8767E-03	4.6800E-03	4.6727E-03	4.6803E-03	4.7011E-03
20	4.4462E-03	5.5800E-03	4.4436E-03	4.4366E-03	4.4438E-03	4.4636E-03
21	3.8863E-03	4.8774E-03	3.8840E-03	3.8779E-03	3.8842E-03	3.9015E-03
22	3.5691E-03	4.4793E-03	3.5670E-03	3.5613E-03	3.5671E-03	3.5830E-03
23	3.2931E-03	4.1330E-03	3.2912E-03	3.2860E-03	3.2913E-03	3.3060E-03
24	3.1581E-03	3.9635E-03	3.1563E-03	3.1513E-03	3.1564E-03	3.1705E-03
25	4.1970E-02	5.2674E-02	4.1946E-02	4.1879E-02	4.1947E-02	4.2134E-02

Table VII. Dose Fraction Versus Ion Charge Number and Relative Integration Error for Neon Ions Incident Upon Atmosphere

[E_o = 1000 MeV/nucleon]

Ion charge number	Dose fraction for relative integration error of—			
	10^{-2}	10^{-4}	10^{-6}	10^{-8}
1	5.6956E-01	5.6942E-01	5.7009E-01	5.7009E-01
2	1.2701E-01	1.2707E-01	1.2687E-01	1.2687E-01
3	6.3886E-02	6.3906E-02	6.3806E-02	6.3806E-02
4	4.4419E-02	4.4431E-02	4.4362E-02	4.4362E-02
5	3.3100E-02	3.3108E-02	3.3056E-02	3.3056E-02
6	2.7910E-02	2.7916E-02	2.7873E-03	2.7873E-02
7	2.2359E-02	2.2364E-02	2.2329E-02	2.2329E-02
8	1.8430E-02	1.8434E-02	1.8406E-02	1.8406E-02
9	1.4762E-02	1.4767E-02	1.4744E-02	1.4744E-02
10	7.8566E-02	7.8585E-02	7.8463E-02	7.8463E-02

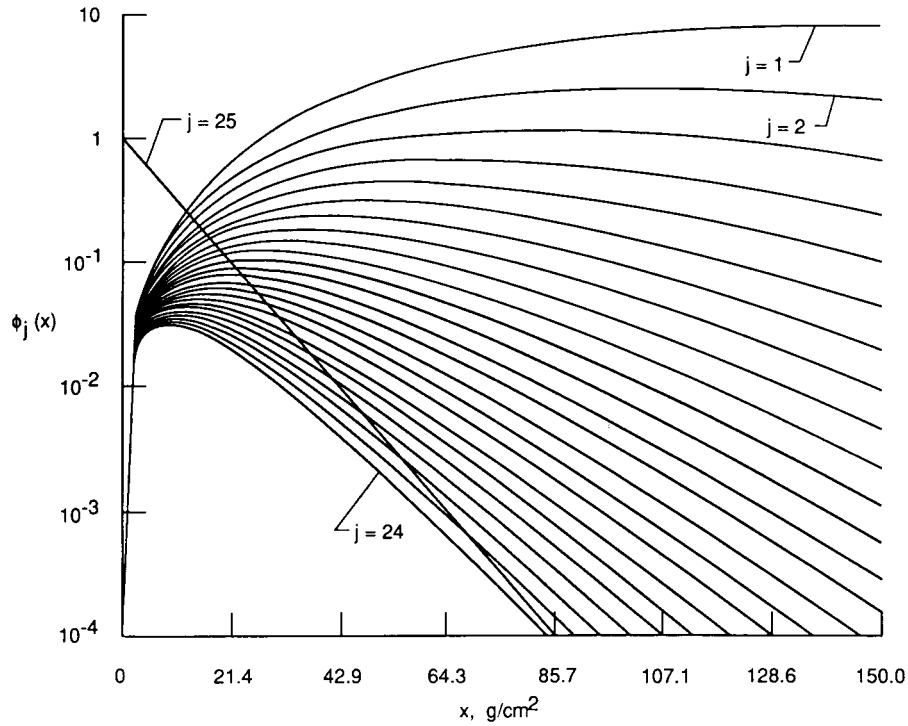

(a) Spatial variation of ion fluxes. $j = 1,\ 2,\ \ldots,\ 25$.

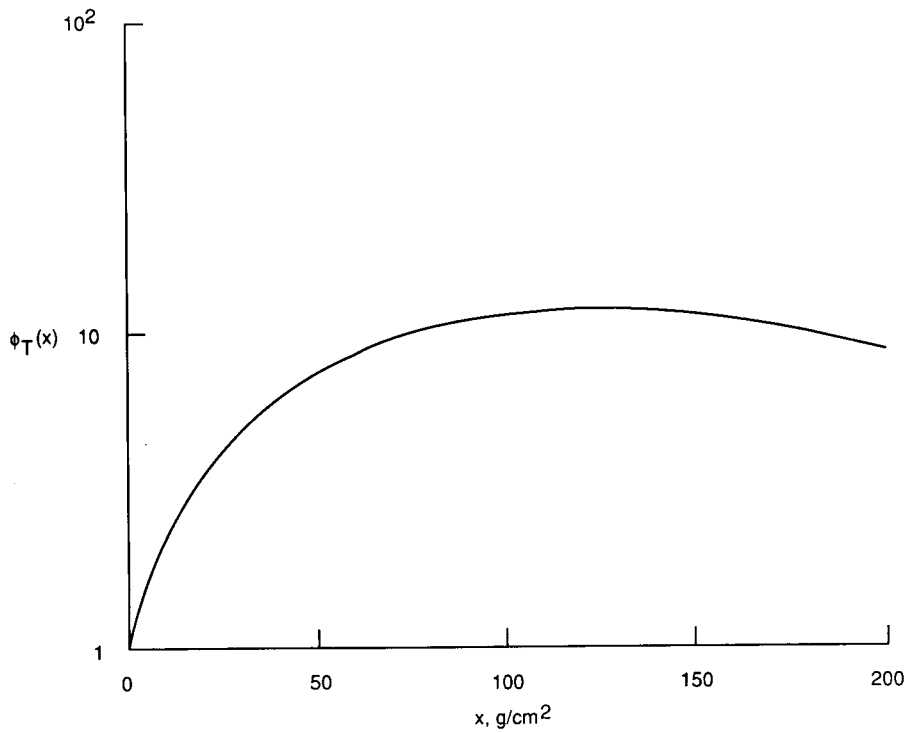

(b) Variation of $\phi_T(x)$ with x.

Figure 1. Physical trends for flux.

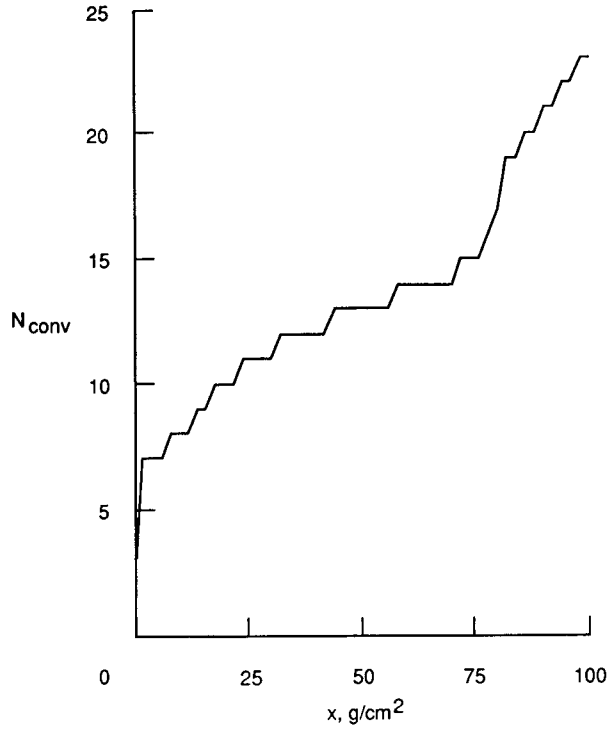

(a) Single layer.

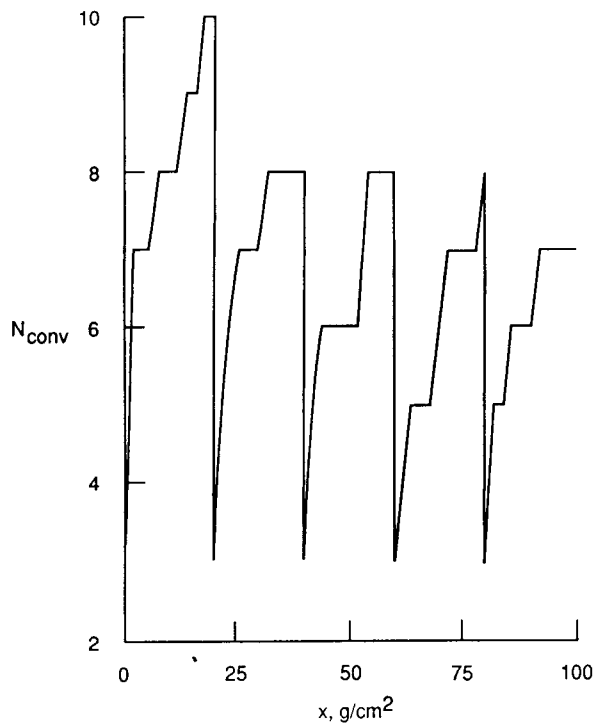

(b) Five layers.

Figure 2. Number of terms required for convergence.

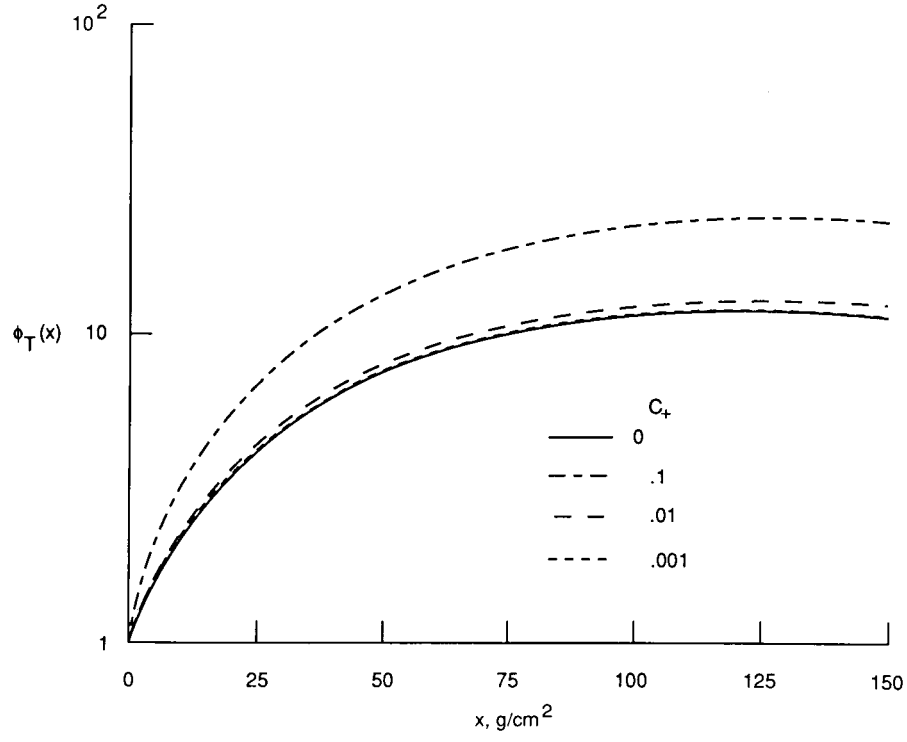

Figure 3. Variation of $\phi_T(x)$ including ion $J+1$.

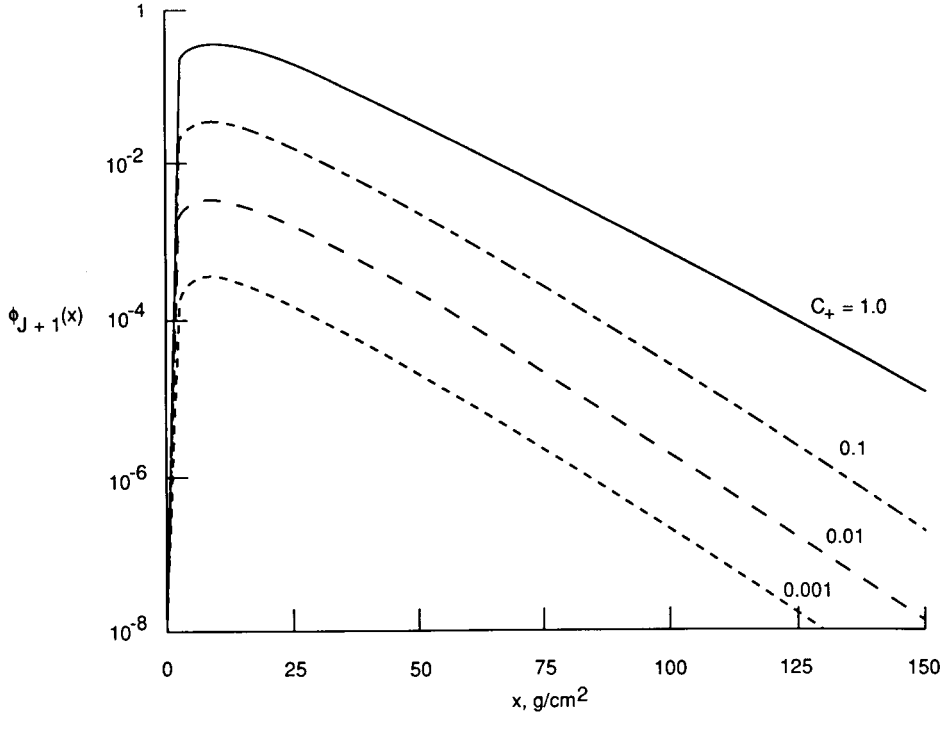

Figure 4. Variation of ion $J+1$ flux.

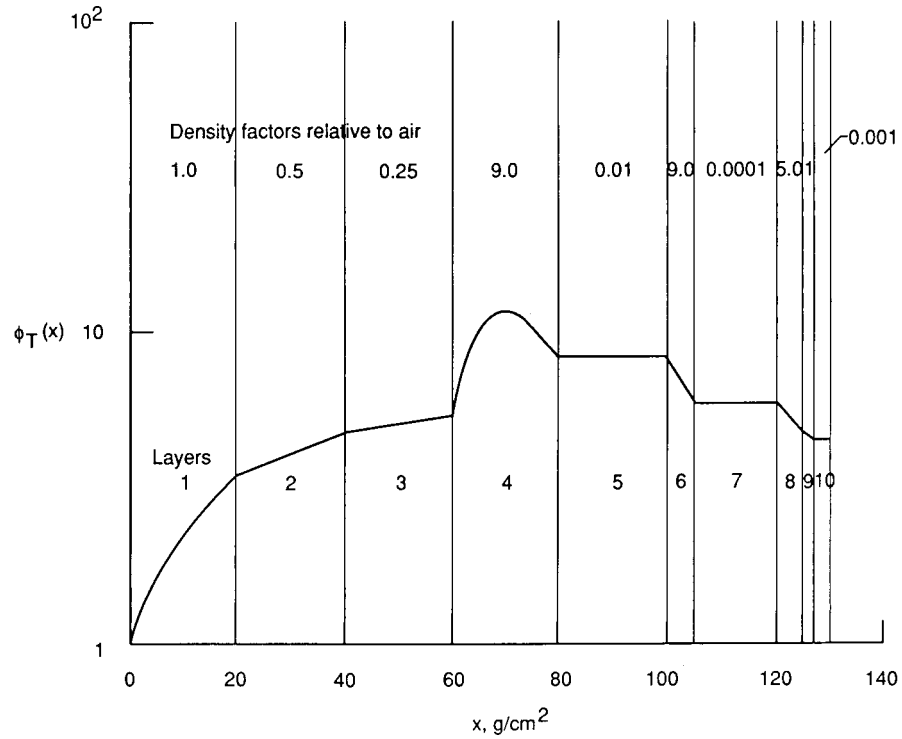

Figure 5. Total flux for multiple shields.

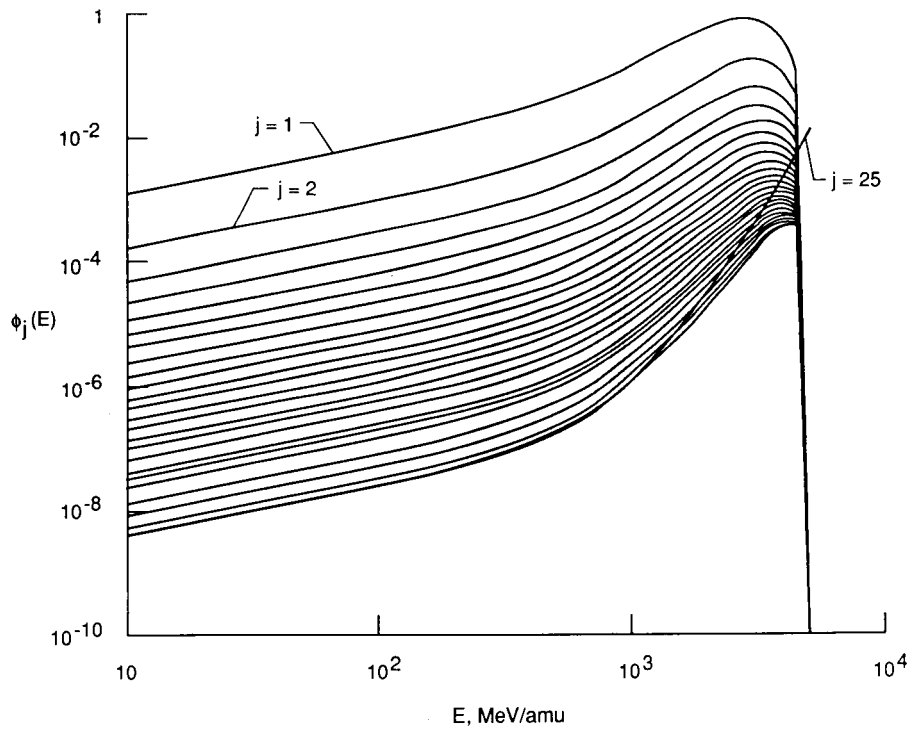

Figure 6. Ion flux variation with E.

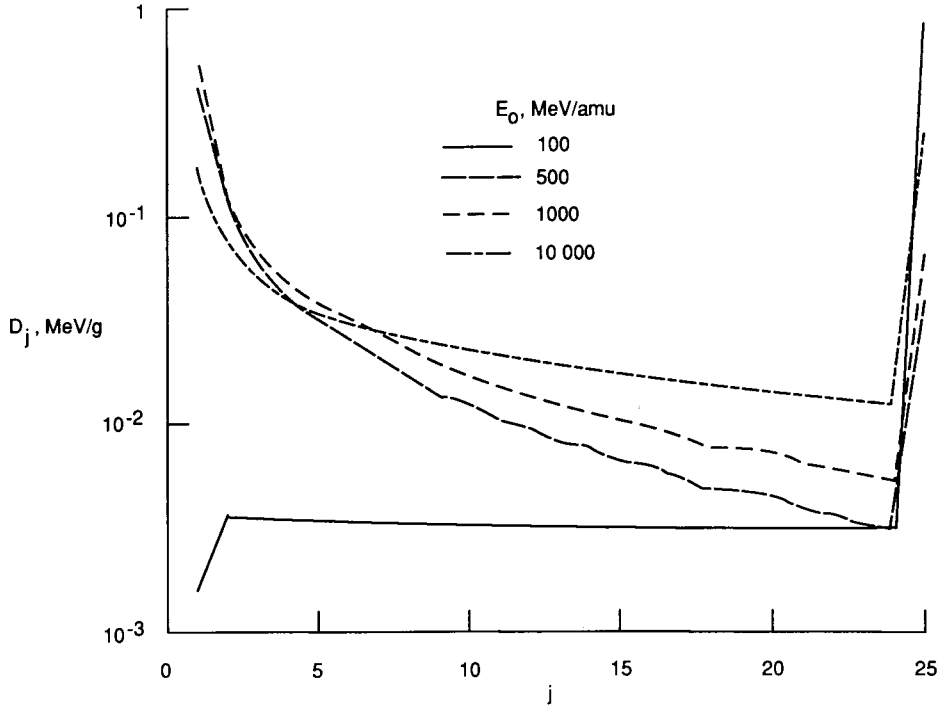

Figure 7. Dose variation with E_0 for $J = 25$.

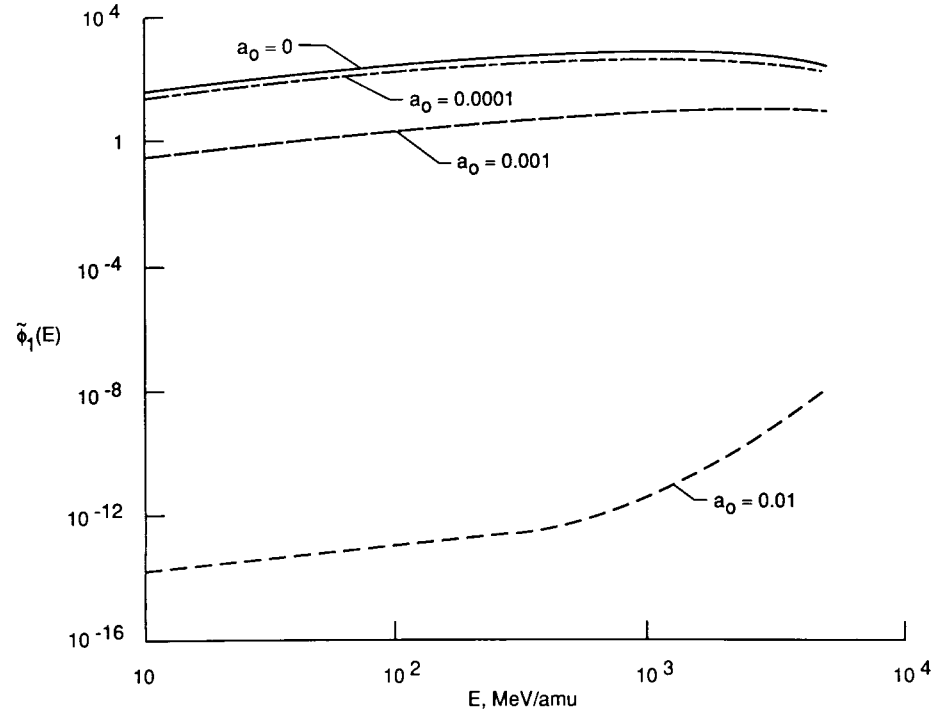

Figure 8. Flux of ion $j = 1$ for various decay constants a_o of exponential source. $J = 25$; $E_o = 1000$ MeV/amu.

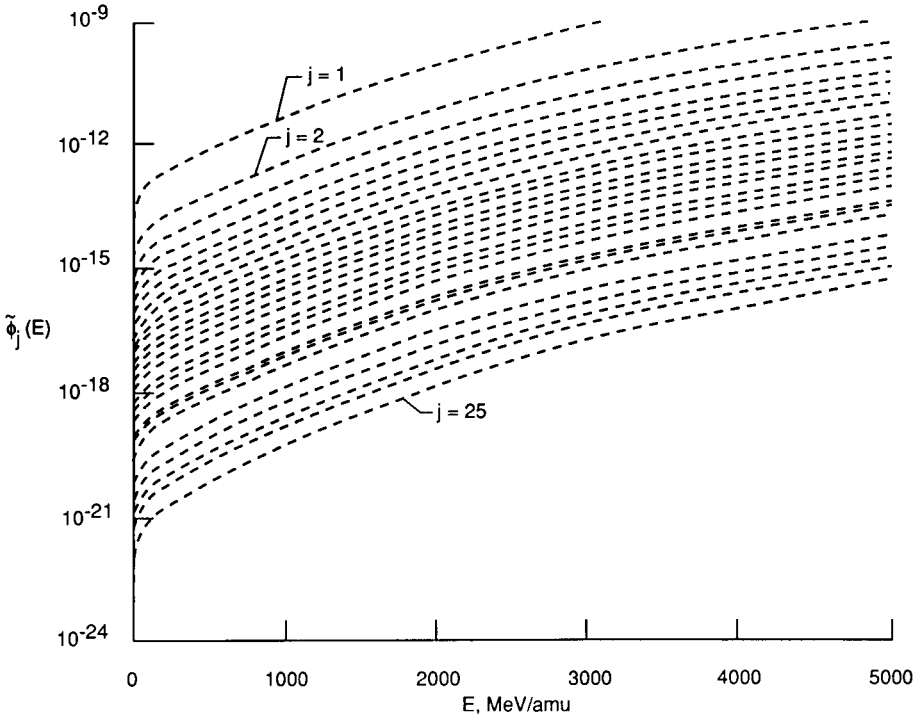

Figure 9. Variation of $\tilde{\phi}_j(E)$ with E. $Q(E) = Q_o \exp(-a_o s)$; $a_n = 0.01$.

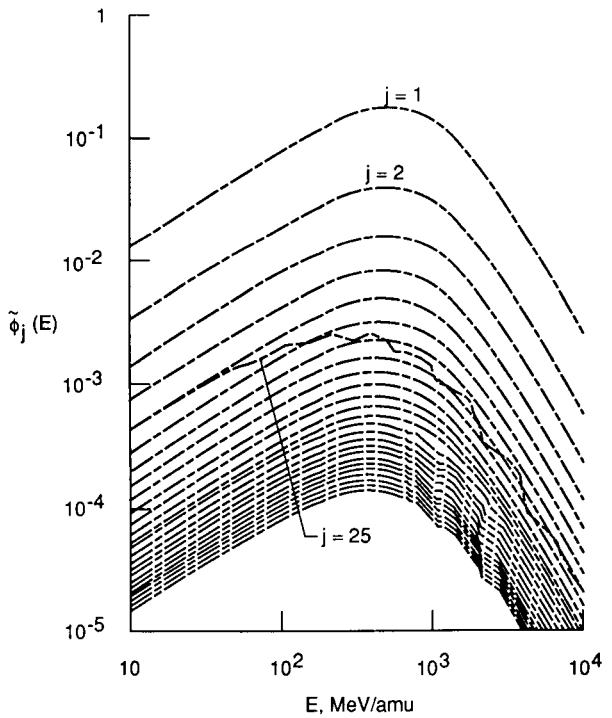

(a) 15 intervals; 2 points/interval.

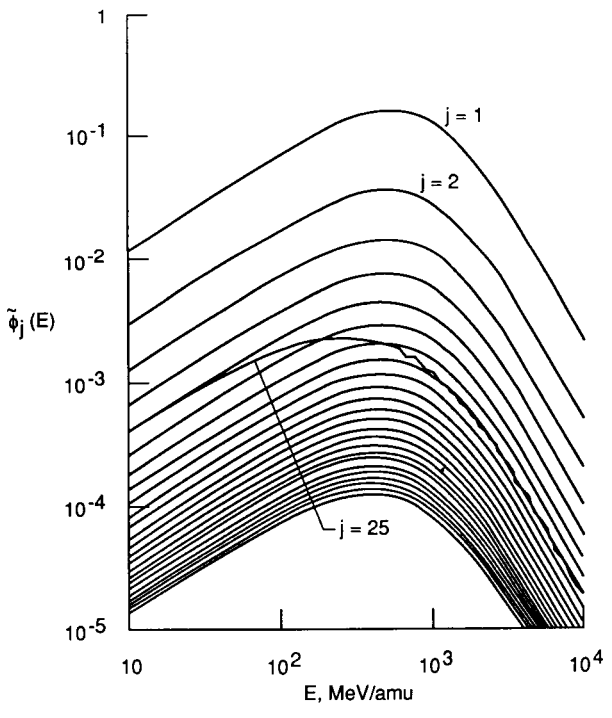

(b) 40 intervals; 2 points/interval; $E_o = 10\,000$.

Figure 10. Flux variation from analytical solution with solar source.

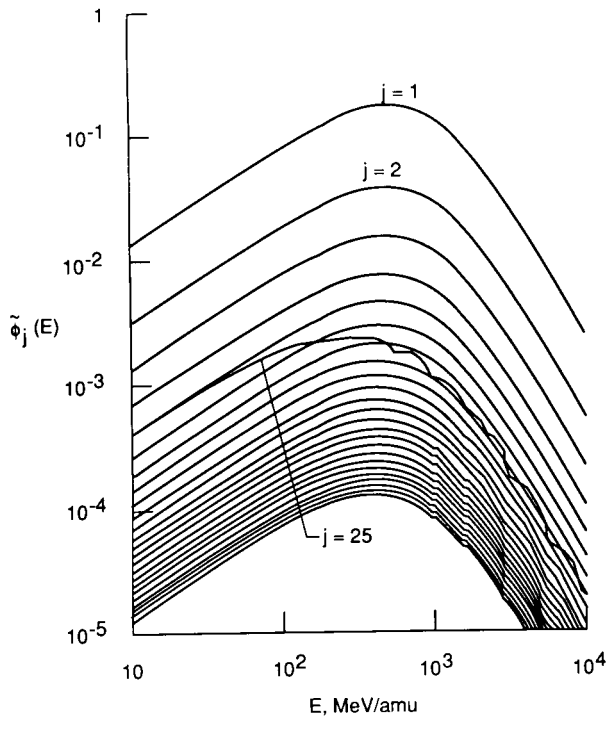

(a) Constant.

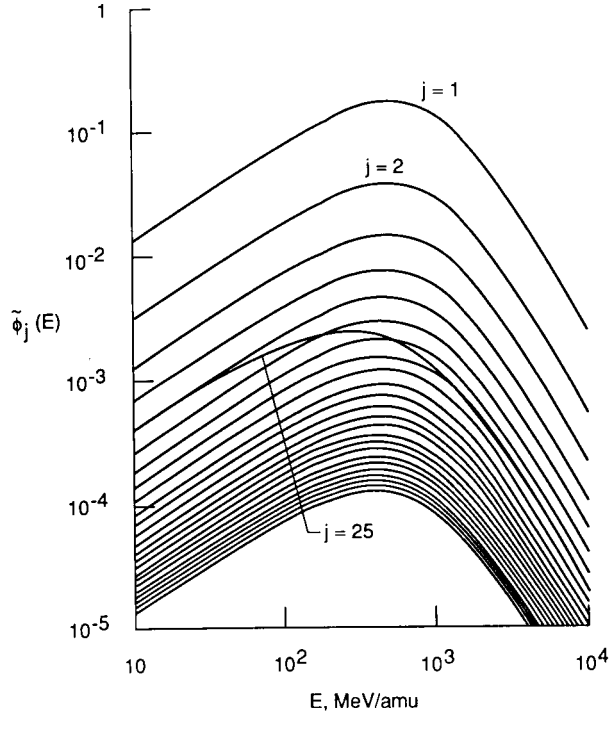

(b) Linear.

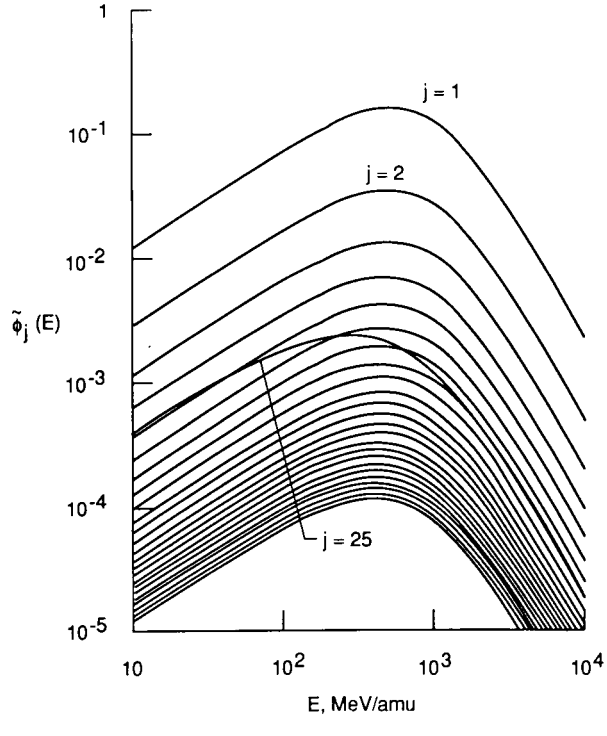

(c) Quadratic.

Figure 11. Flux variation from power series method with solar source. 15 intervals; 2 points/interval.

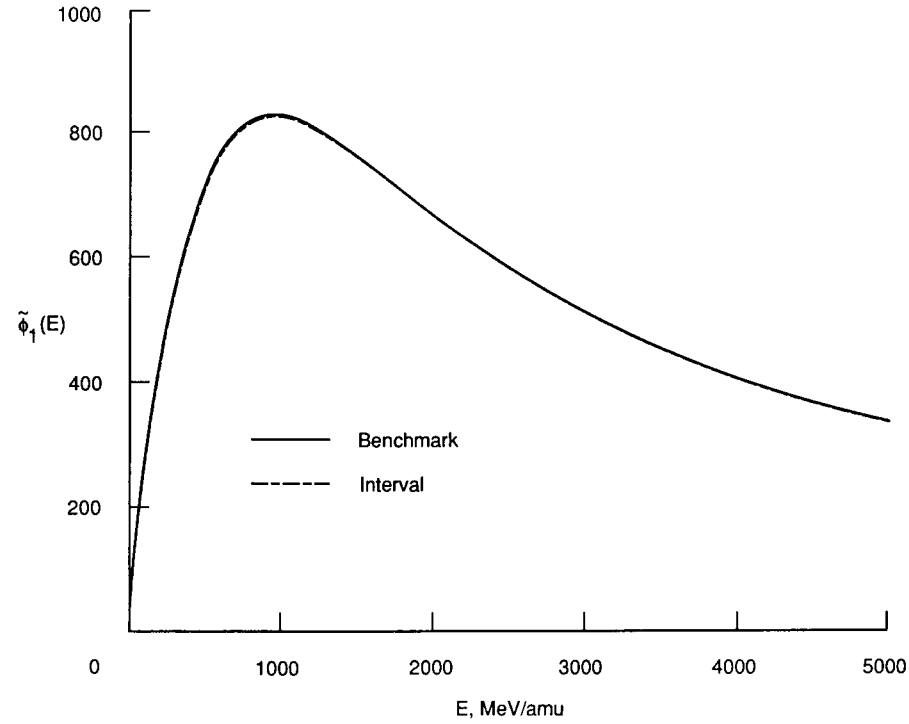

(a) $a_o = 0.$

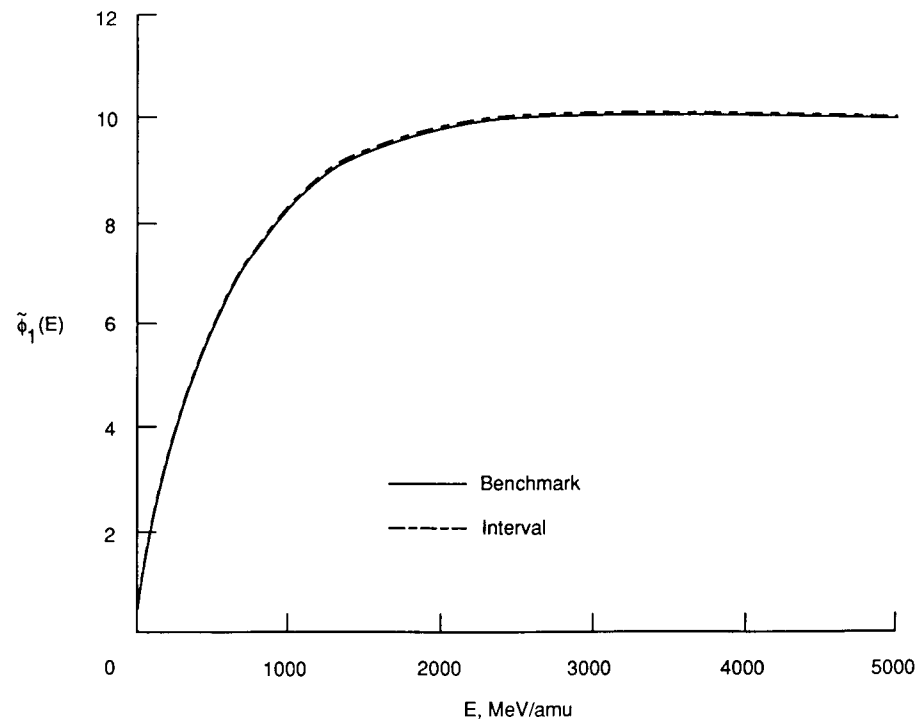

(b) $a_o = 0.001.$

Figure 12. Benchmark and interval calculations for ϕ_1.

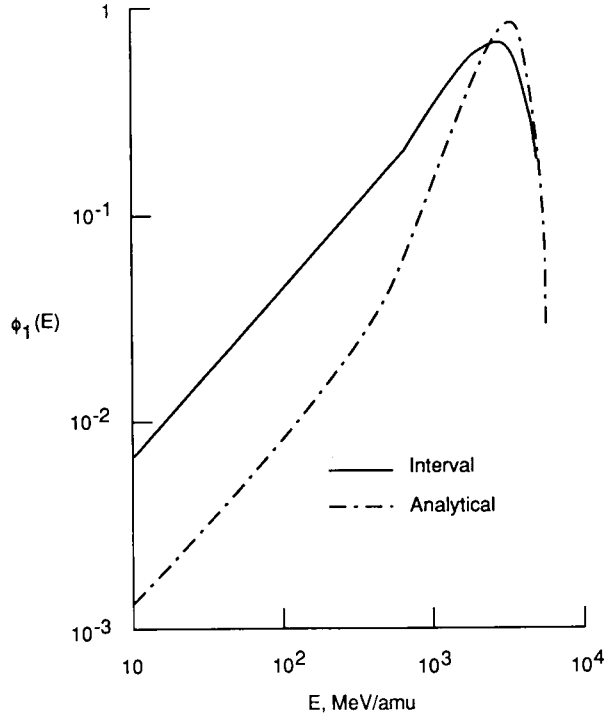

(a) $N_p = 10$.

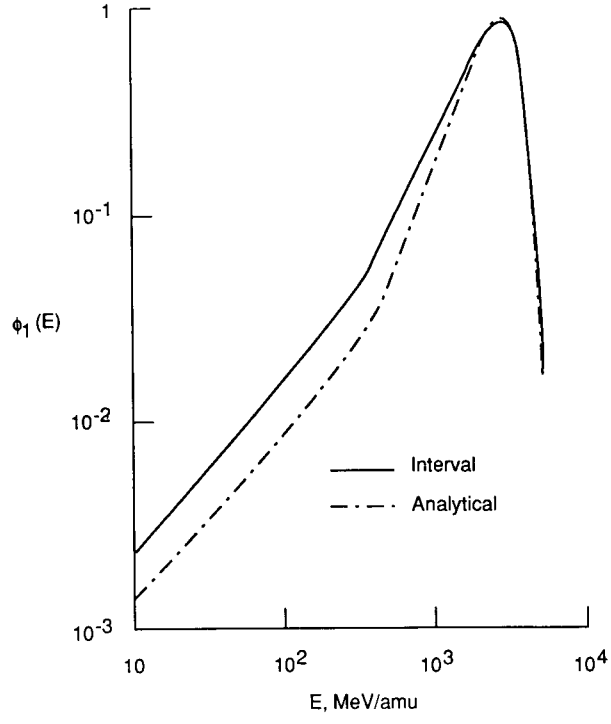

(b) $N_p = 50$.

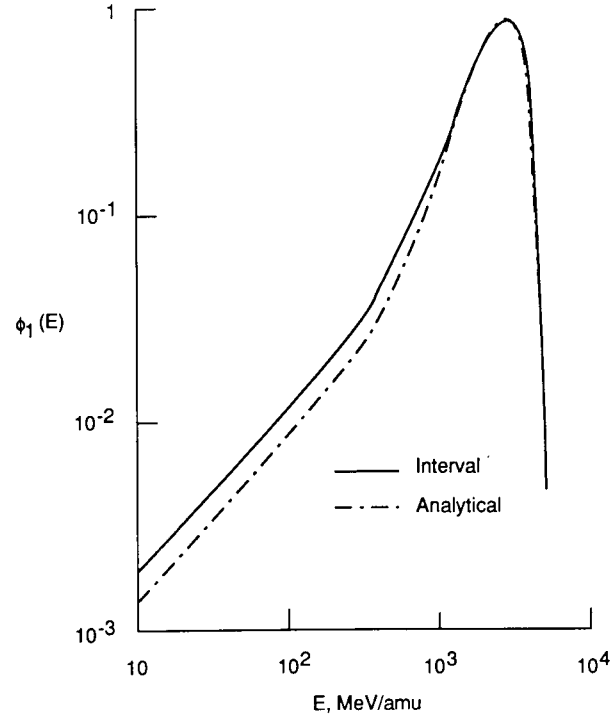

(c) $N_p = 100$.

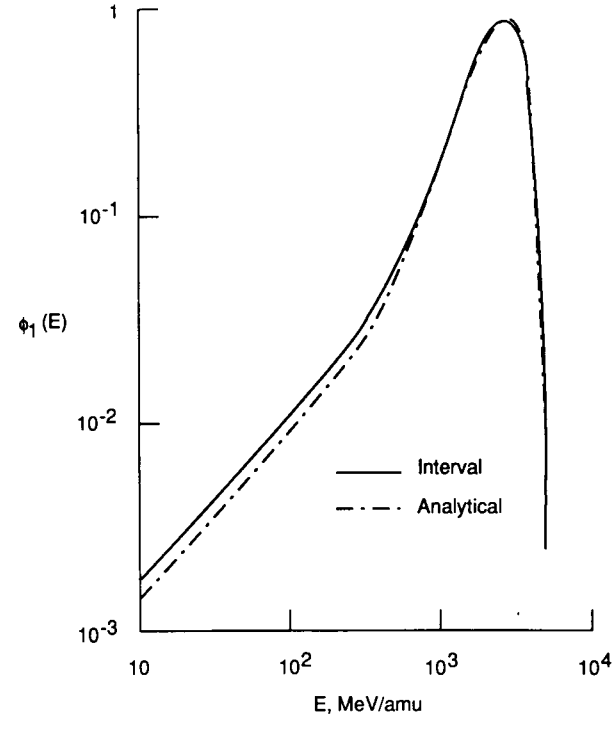

(d) $N_p = 150$.

Figure 13. Analytical and interval solutions for ϕ_1. $J = 25$; $E_o = 5$ GeV/amu.

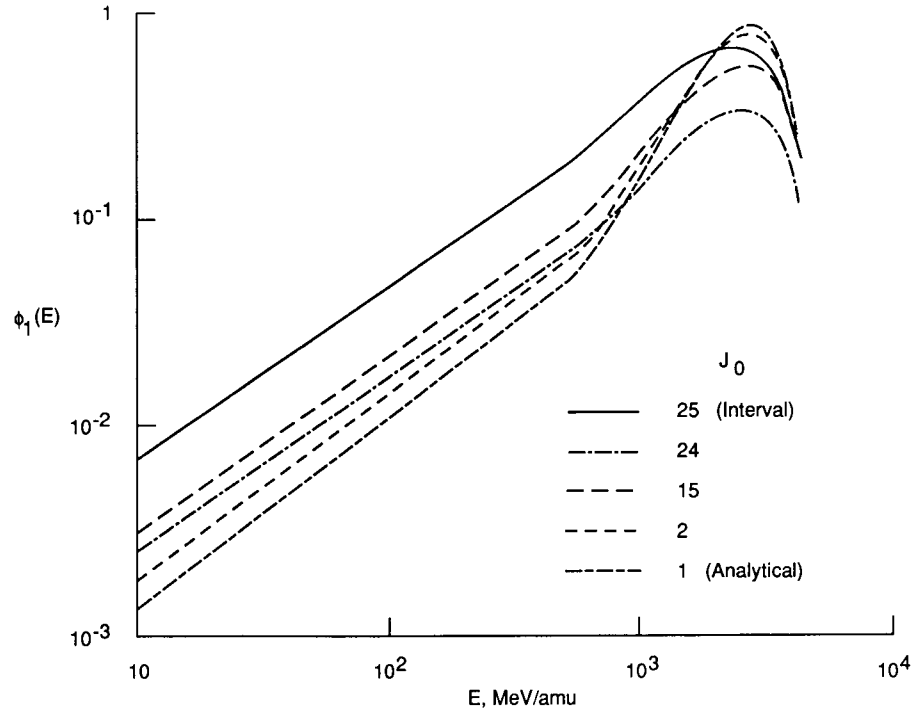

Figure 14. Analytical-interval hybrid scheme for ϕ_1. $N_p = 10$.

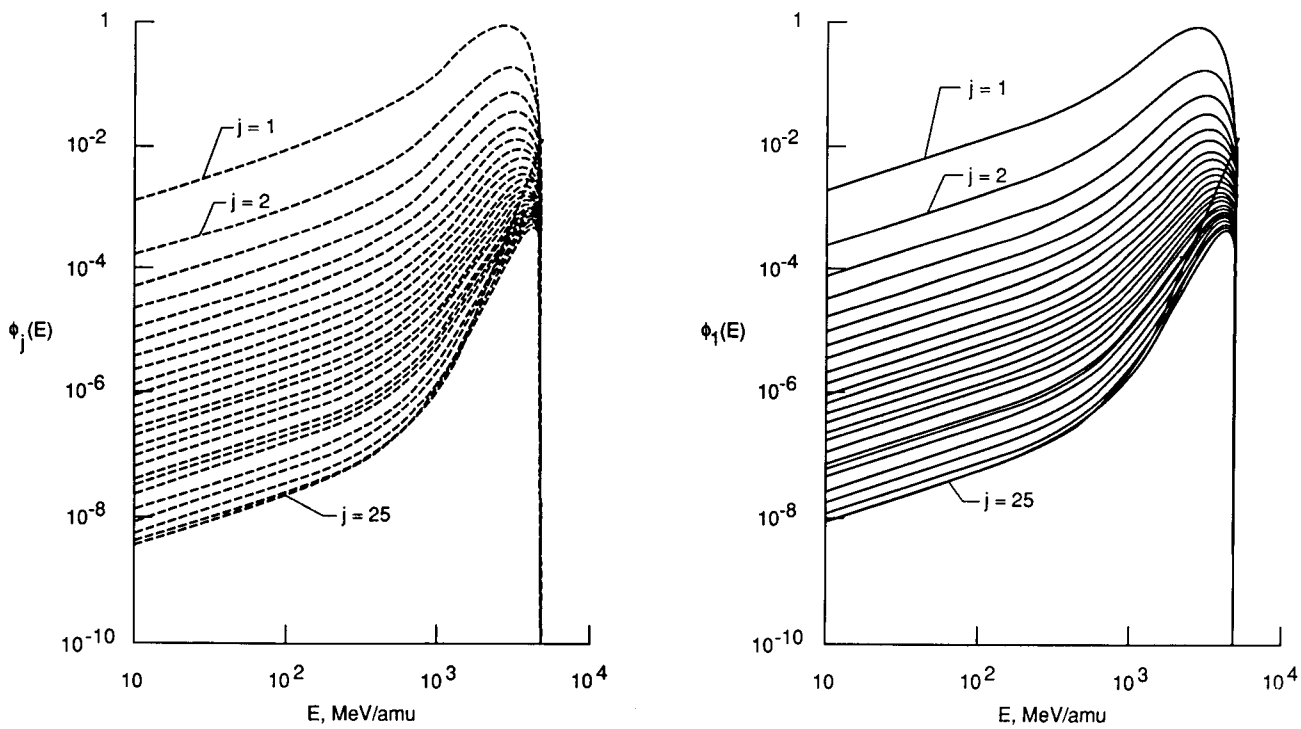

(a) Interval ($N_p = 100$).

(b) Analytical.

Figure 15. Complete spectra for analytical and interval solutions.

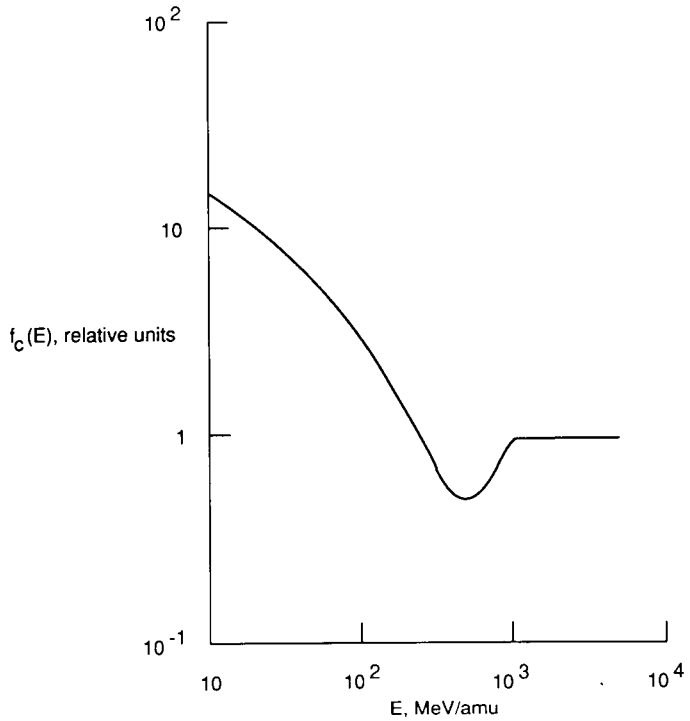

Figure 16. Energy-dependent cross-section shape.

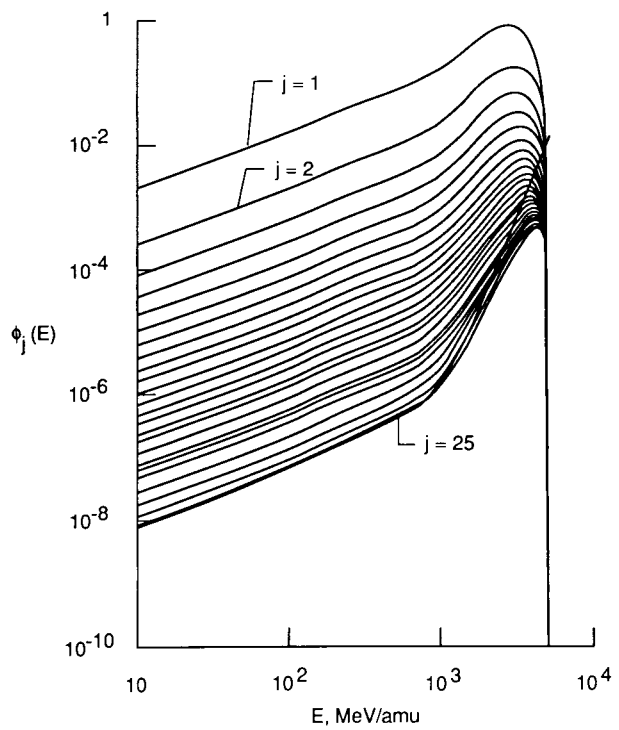

(a) With energy dependence.

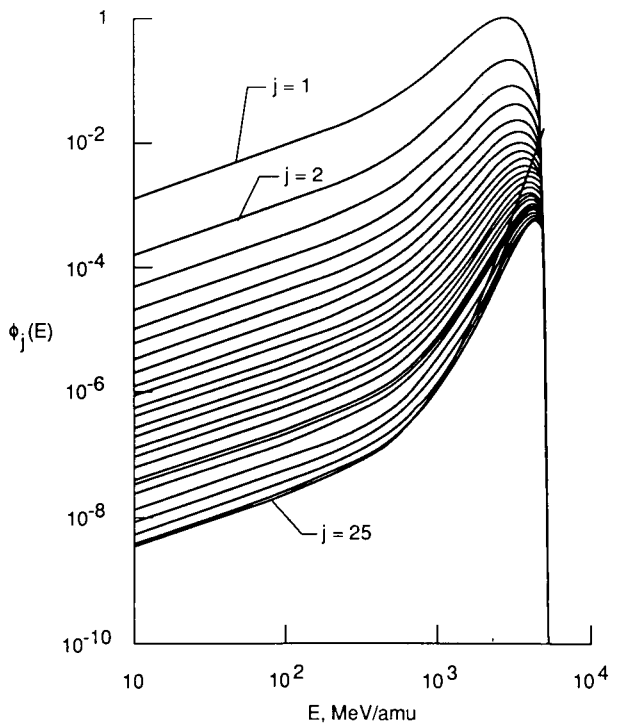

(b) Without energy dependence.

Figure 17. Flux variation with and without energy dependence of absorption cross section.

NASA
National Aeronautics and Space Administration

Report Documentation Page

1. Report No.	2. Government Accession No.	3. Recipient's Catalog No.
NASA TP-2878		

4. Title and Subtitle	5. Report Date
Benchmark Solutions for the Galactic Ion Transport Equations: Energy and Spatially Dependent Problems	March 1989
	6. Performing Organization Code
7. Author(s)	8. Performing Organization Report No.
Barry D. Ganapol, Lawrence W. Townsend, and John W. Wilson	L-16519
9. Performing Organization Name and Address	10. Work Unit No.
NASA Langley Research Center Hampton, VA 23665-5225	199-22-76-01
	11. Contract or Grant No.
12. Sponsoring Agency Name and Address	13. Type of Report and Period Covered
National Aeronautics and Space Administration Washington, DC 20546-0001	Technical Paper
	14. Sponsoring Agency Code

15. Supplementary Notes

Barry D. Ganapol: University of Arizona, Tucson, Arizona.
Lawrence W. Townsend and John W. Wilson: Langley Research Center, Hampton, Virginia.

16. Abstract

Nontrivial benchmark solutions are developed for the galactic ion transport (GIT) equations in the straight-ahead approximation. These equations are used to predict potential radiation hazards in the upper atmosphere and in space. Two levels of difficulty are considered: (1) energy independent and (2) spatially independent. The analysis emphasizes analytical methods never before applied to the GIT equations. Most of the representations derived have been numerically implemented and compared with more approximate calculations. Accurate ion fluxes (to 3 to 5 digits) are obtained for nontrivial sources. For monoenergetic beams, both accurate doses and fluxes are found. The benchmarks presented herein are useful in assessing the accuracy of transport algorithms designed to accommodate more complex radiation protection problems. In addition, these solutions can provide fast and accurate assessments of relatively simple shield configurations.

17. Key Words (Suggested by Authors(s))	18. Distribution Statement
Benchmark solutions Heavy-ion transport Space radiation	Unclassified—Unlimited Subject Category 93

19. Security Classif. (of this report)	20. Security Classif. (of this page)	21. No. of Pages	22. Price
Unclassified	Unclassified	29	A03

NASA FORM 1626 OCT 86 NASA-Langley, 1989
For sale by the National Technical Information Service, Springfield, Virginia 22161-2171